

THE MATRYOSKA RUN: EULERIAN REFINEMENT STRATEGY TO STUDY STATISTICS OF TURBULENCE IN VIRIALIZED COSMIC STRUCTURES

FRANCESCO MINIATI

Physics Department, Wolfgang-Pauli-Strasse 27, ETH-Zürich, CH-8093, Zürich, Switzerland; fm@phys.ethz.ch

Draft version October 5, 2018

ABSTRACT

We study the statistical properties of turbulence driven by structure formation in a massive merging galaxy cluster at redshift $z=0$. The development of turbulence is ensured as the largest eddy turnover time is much shorter than the Hubble time independent of mass and redshift. We achieve a large dynamic range of spatial scales through a novel Eulerian refinement strategy where the cluster volume is refined with progressively finer uniform nested grids during gravitational collapse. This provides an unprecedented resolution of $7.3 \text{ h}^{-1} \text{ kpc}$ across the virial volume. The probability density functions of various velocity derived quantities exhibit the features characteristic of fully developed compressible turbulence observed in dedicated periodic-box simulations. Shocks generate only 60% of the total vorticity within $R_{\text{vir}}/3$ region and 40% beyond that. We compute second and third order, longitudinal and transverse, structure functions for both solenoidal and compressional components, in the cluster core, virial region and beyond. The structure functions exhibit a well defined inertial range of turbulent cascade. The injection scale is comparable to the virial radius but increases towards the outskirts. Within $R_{\text{vir}}/3$, the spectral slope of the solenoidal component is close to Kolmogorov's, but for the compressional component is substantially steeper and close to Burgers'; the flow is mostly solenoidal and statistically rigorously consistent with fully developed, homogeneous and isotropic turbulence. Small scale anisotropy appears due to numerical artifact. Towards the virial region, the flow becomes increasingly compressional, the structure functions flatter and modest genuine anisotropy appear particularly close to the injection scale. In comparison, mesh adaptivity based on Lagrangian refinement and the same finest resolution, leads to lack of turbulent power on small scale and excess thereof on large scales, with the discrepancy growing towards the outer cluster regions, while producing unreliable density weighted structure functions throughout.

Subject headings: large-scale structure of Universe – galaxies: cluster: general – hydrodynamics – turbulence – methods: numerical

1. INTRODUCTION

1.1. Modeling Turbulence

Astrophysical flows are characterized by large Reynolds numbers, $\text{Re} \equiv \frac{uL}{\nu_k}$, where L and u are the characteristic spatial scale and velocity of the fluid motions, respectively, and ν_k the kinematic viscosity. A large Re implies the existence of a wide range of spatial scales where the fluid interactions are dominated by the nonlinear term in Euler's equation, while momentum diffusion remains negligible. This leads to the cascade of fluid motions predominantly from larger to smaller scales, thus generating turbulence (Landau & Lifshitz 1987). Turbulence affects the qualitative behavior of a fluid by adding new features to it. To mention a few, turbulent random motions alter the stability of a self-gravitating fluid by contributing an additional effective pressure (Chandrasekhar 1951; Schmidt et al. 2013). In a compressible isothermal flow, they also generate density peaks which may turn gravitationally unstable (Elmegreen & Scalo 2004; Schmidt et al. 2010; Konstandin et al. 2012). Turbulence modifies the transport coefficient of a fluid, e.g. the diffusion of scalar quantities such as temperature, entropy and metals (e.g. Zel'dovich et al. 1990). Turbulence strongly amplifies magnetic field (e.g. Zel'dovich et al. 1983; Biskamp 1993; Cho & Yoo 2012; Federrath et al. 2011; Beresnyak 2012). It is argued that turbulence changes the funda-

mental workings of magnetic reconnection in astrophysical plasma (Lazarian & Vishniac 1999; Lazarian et al. 2012). For these and many other reasons the role of turbulence is investigated in several subjects of physics and astrophysics, ranging from the earth's upper atmosphere, the sun, the interstellar medium and molecular clouds of galaxies, and galaxy clusters.

An important effort in the study of turbulence concerns the determination of the structure of the fluid quantities as produced by the turbulent cascade. Numericists pursue this effort using large (magneto) hydrodynamical simulations, with periodic boundary conditions, in which the turbulence is driven on as large a scale as allowed by the computational box, in order to maximize the dynamic range of spatial scales. The turbulence is studied under variety of conditions including, amongst others, incompressible and compressible flows, steady state and decaying regime, solenoidal and/or compressible forcing (Federrath et al. 2008; Federrath 2013), isothermal or adiabatic-law equation of state. This is partly motivated by the variety of conditions that apply to different astrophysical systems. The aim is to understand the fundamental properties of the turbulence, including the scaling relations that apply to velocity and other thermodynamic variables and, related to this, the structures responsible for energy dissipation. One may then wish to use this understanding to properly model actual astrophysical objects in accord with their physical conditions.

Models of driven turbulence in periodic boxes reduce to a minimum the complications associated with boundary effects and, provided numerical convergence, they allow for a clean interpretation of the results.

It is also important, however, to have the ability to model the turbulent flows directly in the actual astrophysical context and environment. This allows to produce more realistic conditions under which the turbulence develops. In particular, the forcing terms may not necessarily operate on a narrow range of scales, may include a combination of solenoidal and compressible terms, may very well be time dependent. The flow itself may be self-gravitating and non homogeneous. So, while the periodic-box studies remain instrumental for the analysis of the results, there is value in modeling the turbulence under the proper astrophysical conditions. This, of course, has remained of limited applicability because of the considerable numerical requirements, as turbulence does not develop unless the Re of the flow is large enough.

With the foregoing objectives in mind, in this paper we attempt to study the statistical properties of the turbulence in the intracluster medium (ICM) of a massive galaxy cluster (GC). In particular we use a high resolution hydrodynamical simulation of structure formation to compute probability distributions function and structure functions of various velocity fields to establish the genuine turbulent character of the fluid motions inside the GC volume. Here we focus on a purely hydrodynamic model (the magnetic field is present but completely negligible for the dynamics) and leave the case of saturated magneto-hydrodynamical turbulence to future work.

Applying mesh adaptivity based on Lagrangian refinement criterion produces high resolution in only a small fraction of the volume. This results in well resolved collapsed structures but the effective Re of the flow remains poor. So while large eddies appear, turbulence cannot develop. To obviate this and achieve a sufficiently large range of well resolved spatial scales across the GC volume we employ instead a novel Eulerian refinement approach, providing uniform high spatial resolution throughout the GC volume. Uniform resolution also avoids biases in the statistics and allows us to carry out the analysis as closely as possible to the periodic-box cases.

There are several previous numerical studies of turbulence in the ICM but with very different focus (see below). The work of Vazza et al. (2009, 2011) is closest to ours in terms of purposes although there are still differences in terms of peak resolution and dynamic range, resolution strategy and analysis. Analogous efforts in other fields include the study of three-dimensional convective turbulence in the stratified atmosphere of stars (Porter & Woodward 2000; Viallet et al. 2013) and the magneto-rotational instability in the magnetized accretion disks (Bodo et al. 2011; Parkin & Bicknell 2013).

1.2. Turbulence in Galaxy Clusters

Galaxy clusters (GC), with mass up to a few $\times 10^{15} M_{\odot}$, are the largest virialized systems, sitting at the top of the hierarchical chain of cosmic structure. They grow hierarchically, through mergers with other already collapsed systems, and also through smooth accretion of matter that is still far from virialization. Massive GC are still dynamically young and in the process of formation. As

a result, they have yet to reach fully relaxed dynamical conditions. Most of the baryonic mass is in a state of fully ionized hot plasma namely the ICM, with number density and temperature in the range, $n_e \sim 10^{-2} - 10^{-5} \text{ cm}^{-3}$ and, $T \sim 10^7 - 10^8 \text{ K}$, respectively, from the core to the outskirts region.

From the hydrodynamical point of view both the merger process and smooth accretion play important roles (see also Sec. 3.2). Mergers set up large scale motions in the ICM, which eventually dissipate through turbulent cascade or shocks of various strength. Smooth accretion occurring through filaments typically penetrates inside GC down to a fraction of the virial radius depending on the filament size, generating large scale shear flows and shocks at the filament-ICM interface. Smooth accretion from voids is hypersonic and produces very high Mach number shocks with curvature radii of a few Mpc. As shown later (Sec. 3.1.2) these shocks are characterized by highly irregular surface and only partially dissipate the kinetic energy of the accreting gas. Owing to their curvature, they generate large scale vorticity, thus acting as an additional sources of turbulence.

The development of turbulence relies on large Re . This depends on the mean free path of thermal particles in the ICM which is somewhat subject to debate. Magnetic fields, however, are commonly observed in the ICM (Clarke et al. 2001; Clarke 2004; Feretti & Johnston-Hollitt 2004). So it is assumed here that the mean free path is determined by the Larmor radius in the direction perpendicular to the magnetic field, and by microscopic (e.g. mirror and firehose) plasma instabilities along the mean magnetic field lines (Parker 1958; Ginzburg 1979; Schekochihin et al. 2005), although the simulation resolution never reaches scales below the Coulomb mean free path in the ICM. The important thing is that, irrespective of the specific viscosity mechanism, using 10^3 km s^{-1} for the typical flow velocity and a Mpc for the characteristic spatial scales (Sec. 3.2) leads to large enough Re ($\gtrsim 10^3$) for the onset of turbulent motions throughout the GC volume.

The properties of turbulence in the GC are important for a variety of reasons. Support against gravity from turbulence as well as bulk motions introduces biases in the GC mass estimates based on the assumption of hydrostatic equilibrium (Faltenbacher et al. 2005; Dolag et al. 2005; Lau et al. 2009; Nagai et al. 2007; Biffi et al. 2011; Valdarnini 2011), with important consequence for the use of GC as cosmological probes. Characterizing the turbulence allows us to determine the expected level equipartition between magnetic and kinetic energy in the ICM and shed light on the origin of magnetic fields there (Subramanian et al. 2006; Iapichino & Niemeyer 2008). Cluster turbulence affects the transport of relativistic particles both in momentum and configuration space, and is studied also to understand the origin of cluster diffuse radio sources (Paul et al. 2011; Hallman & Jeltrema 2011; Vazza et al. 2009, 2011).

Observations of turbulence in the ICM are, however, extremely challenging. To first attempt to determine the presence of turbulent motions on a range of scales in the ICM is due to Schuecker et al. (2004). These authors used X-ray XMM-Newton observations of the

nearby massive Coma GC, to measure the pressure fluctuations induced by turbulent motions in an incompressible fluid (Kolmogorov 1941a,b; Oboukhov 1941). The presence and spectral properties of turbulence have also been probed via the analysis of the structure of rotation measure (RM) maps, of extended radio sources typically embedded in the ICM (Enßlin & Vogt 2003; Kuchar & Enßlin 2011), leading to results consistent with a Kolmogorov spectrum.

In fact, turbulent motions imprint a number of features on the ion emission lines due to Doppler effect, such as profile broadening and centroid shifting (e.g. Sunyaev et al. 2003). For heavy ions these effects dominate over thermal broadening ($\propto 1/m_{ion}^{1/2}$), opening a new observational window on the properties of turbulent motions (Inogamov & Sunyaev 2003; Zhuravleva et al. 2011, 2012). This science will become possible with the advent of high precision X-ray spectrometers, such as Astro-H¹ and Athena², which will have energy resolution of a few eV, allowing to measure gas motions of order 100 km/s in massive clusters. Currently, Doppler broadening of iron emission lines is employed to probe turbulent motions in cool cores, where thermal motions are particularly low (Churazov et al. 2008; Sanders et al. 2010, 2011). Alternatively, the presence of turbulent gas motions in the ICM (of Perseus cluster) has been inferred from the lack of resonant scattering effects for the He-like iron emission line at 6.7 keV (Churazov et al. 2004).

The rest of this paper is organized as follows. Full details of the numerical calculation, including the code, the initial condition, the cosmological model and the refinement strategy, are described in detail in Sec. 2. The main results, in particular the analysis of the simulations in terms of two-dimensional plots, probability density functions, and various velocity structure functions, convergence analysis and comparison with Adaptive-Mesh-Refinement, are presented in Sec. 3. The discussion in Sec. 4 concludes the paper.

2. NUMERICS

2.1. Code, Cosmology and Initial Conditions

The simulation of structure formation is carried out with the Adaptive-Mesh-Refinement cosmological code CHARM (Miniati & Colella 2007). We use a directionally unsplit variant of the Piecewise-Parabolic-Method for hydrodynamics (Colella 1990), a time centered modified symplectic scheme for the collisionless dark matter and solve Poisson's equation with a second order accurate discretization (Miniati & Colella 2007). In addition to hydrodynamics and self-gravity, the calculation evolves a dynamically negligible magnetic field using the constrained-transport algorithm for solenoidal MHD described in Miniati & Martin (2011). Radiative cooling and heating of the intergalactic medium through photoionization is neglected. While this results in a lower gas temperature in voids and, in a correspondingly higher Mach number for the outermost accretion shocks, it has no consequences whatsoever for the generation of vorticity and turbulence at shocks.

We assume a concordance Λ -CDM universe with nor-

malized (in units of the critical value) total mass density, $\Omega_m = 0.2792$, baryonic mass density, $\Omega_b = 0.0462$, vacuum energy density, $\Omega_\Lambda = 1 - \Omega_m = 0.7208$, normalized Hubble constant $h \equiv H_0/100 \text{ km s}^{-1} \text{ Mpc}^{-1} = 0.701$, spectral index of primordial perturbation, $n_s = 0.96$, and rms linear density fluctuation within a sphere with a comoving radius of $8 h^{-1} \text{ Mpc}$, $\sigma_8 = 0.817$ (Komatsu et al. 2009).

The initial conditions are generated for a volume of comoving size $L_{Box} = 240 h^{-1} \text{ Mpc}$, sufficiently large to accommodate statistically significant sample of massive clusters at the turnover of the mass function. We use `grafic++`, the parallel version of the `grafic2` package (Bertschinger 2001), developed and made publicly available by D. Potter and the power spectrum interpolation suggested in Eisenstein & Hu (1998).

We carry out a preliminary low resolution run using a uniform grid of 512^3 comoving cells, corresponding to a nominal spatial resolution of $468.75 h^{-1}$ comoving kpc. We sample the distribution function of the collisionless dark matter component with 512^3 particles with mass $6.7 \times 10^9 h^{-1} M_\odot$. At redshift zero halos are identified using our implementation of the HOP halo finder (Eisenstein & Hut 1998), adopting the standard parameters suggested in the original finder paper. A massive GC, with a mass around $10^{15} M_\odot$, is then selected for re-simulation at high resolution.

Zoom-in initial conditions are then generated, using again the `grafic++` code. The matter that ends up inside the simulated massive GC is collected from a Lagrangian volume of about $20 h^{-1}$ comoving Mpc in radius. This volume is initialized at a spatial resolution $\Delta x = 117.2 h^{-1}$ comoving kpc, typically sufficient to resolve structures 100-1000 times smaller than the final GC. To achieve this, we use two additional levels of refinement on top of the base grid. The refinement ratio for both levels is, $n_{ref}^\ell \equiv \Delta x_\ell / \Delta x_{\ell+1} = 2$, $\ell = 0, 1$. Each refined level covers $1/8$ of the volume of the next coarser level with a uniform grid of 512^3 comoving cells. The dark matter distribution function is likewise represented by 512^3 particles on each refined level, so that at the finest level where the initial conditions are generated the particle mass is $1.0 \times 10^8 h^{-1} M_\odot$.

2.2. Eulerian Refinement Strategy

An important objective of our calculation is to resolve with a certain degree of accuracy the inertial range of the turbulent cascade expected to develop in the ICM. The turbulent cascade is initiated at the injection scales, so our aim is to model the turbulent velocity field in a range of scales below injection such that it remains unaffected by numerical viscosity. According to dedicated studies of compressible turbulence, this requires that the scales of interest be resolved with about 32 resolution elements (Porter et al. 1992, 1994, 2002; Federrath et al. 2011). The injection scale of the turbulence, L_{inj} , is expected to be in the range $300\text{-}1000 h^{-1} \text{ kpc}$ (Norman & Bryan 1999; Schuecker et al. 2004; Vazza et al. 2009), therefore we aim for a mesh size on the finest grids of order of a several $h^{-1} \text{ kpc}$, so that turbulent motions above $100 h^{-1} \text{ kpc}$ will be resolved. This requirement is easily achieved if one employs the AMR technique the way it is typically applied in cosmological

¹ <http://astro-h.isas.jaxa.jp>

² <http://sci.esa.int/ixo>

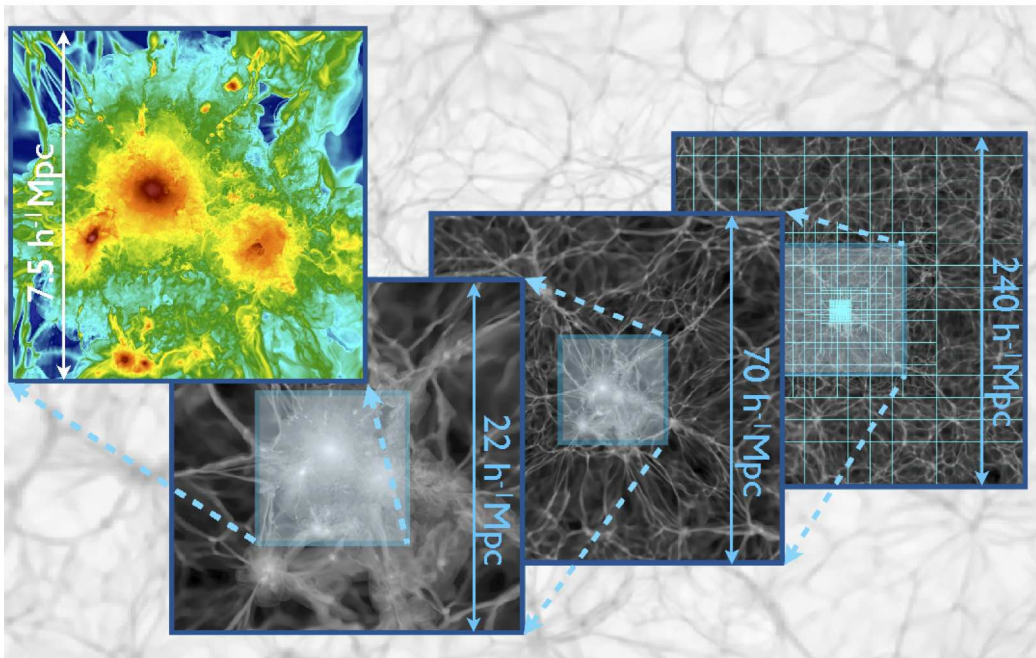


Figure 1. From left to right, panel sequence showing the two dimensional slices of the baryonic gas density distribution in log scale, closing in on the massive GC at the center of the computational volume. The plots correspond to cosmological redshift $z = 0.45$. In the leftmost panel, the full hierarchy of five nested grids with progressively higher resolution is also shown, superposed to the gas density distribution. The translucent bluish-shaded quadrants in the first three panels show the region resolved with finer grids at the next level of refinement. The rightmost panel shows the innermost and highest resolution grid.

simulations, i.e. using a criterion for mesh refinement that is based on mass content of the volume element. We refer to this as Lagrangian flavor of AMR, as it aims at keeping the mass resolution constant, like in particle based Lagrangian codes.

However, this method of refinement is clearly not satisfactory for our purposes because small scales are biased toward high density regions and turbulence will remain unresolved in most of the GC volume. This was already recognized in (e.g. Iapichino & Niemeyer 2008; Paul et al. 2011), where the mass threshold refinement criterion was replaced with one based on the vorticity of the flow, and also in Vazza et al. (2009, 2011) where instead a refinement threshold criterion based on discontinuities of the velocity field was used. As a result of these new refinement criteria, the GC volume fraction covered by high resolution grids increased dramatically.

However, applying finer resolution elements based on the local fluid properties may not necessarily be the best approach. In fact, the AMR technique is of limited computational efficiency when the filling factor is large, e.g. larger than a few 10%, which is certainly the case for fully developed turbulence (Kritsuk et al. 2006). In addition, the presence of coarse/fine grid interfaces introduce numerical error compared to a uniform grids (Berger & Colella 1989). This is not desirable when one is interested in studying the statistical properties, particularly high order ones, of velocity fluctuations associated to turbulence, as it may introduce spurious contribution.

Table 1
Eulerian Refinement Strategy

ℓ	T (H_0^{-1})	L (h^{-1} Mpc)	N_ℓ	n_{ref}^ℓ	Δx_ℓ (h^{-1} kpc)
0	0	240	512	2	468.7
1	0	120	512	2	234.4
2	0	60	512	2	117.2
3	0.013	30	512	4	58.6
4	0.23	15	1024	2	14.6
5	0.48	7.5	1024	-	7.3

Therefore, we have adopted a different approach to achieve the desired high spatial resolution in the GC volume. Basically, we use a set of nested and progressively finer grids that cover uniformly the volume occupied by the simulated GC. The grids are generated dynamically as the Lagrangian volume of the simulated GC shrinks in size under the pull of its self-gravity. We refer to this as Eulerian refinement strategy. Table 1 summarizes the details of our zoom-in simulation. We use a total of 5 levels of refinement. For each level (1), the table report the time of activation (2), the size on a side of the cubic volume covered (3), the number of cells on a side of the uniform grid (4), the refinement ratio with respect to the next finer level (5), and the mesh size (6), respectively. The additional refinement levels (3-5) are employed flexibly as the GC assembles. One can anticipate/delay their activation at the higher/lower cost of a

Table 2
Simulated GC Properties

M_{vir} ($10^{15} M_{\odot}$)	R_{vir} ($h^{-1} \text{Mpc}$)	R_{200} ($h^{-1} \text{Mpc}$)	R_{500} ($h^{-1} \text{Mpc}$)	T (keV)	v_{rms} (km s^{-1})
1.27	1.95	1.5	1	5.2	1927

larger/smaller refined region. Basically a new refinement level is generated when it will be able to accommodate at least two-thirds of the GC Lagrangian volume. In addition, if required, the highest density peaks can also be refined independently based on the Lagrangian refinement criterion, although we did not find this necessary. Note that in most cases a refinement ratio $n_{ref}^{\ell} = 2$ is used, except for level $\ell = 3$, which uses $n_{ref}^3 = 4$, to achieve more efficiently the desired resolution in the GC volume. As shown in Table 1, with our Eulerian refinement strategy we achieve very high, uniform spatial resolution across the virial volume of the simulated GC. This allows us to study in great detail not only the cluster core region, but also the GC outskirts, and determined how the property of the ICM turbulence vary across the virial volume.

Figure 1 shows, as an example, the hierarchy of nested grids when the simulation run has reached approximately redshift 0.4, when the GC is experiencing a major merger. In the leftmost panel, a two dimensional slice of the baryonic gas density distribution is shown in log scale, with superposed the five nested grids of the hierarchy, with sizes listed in Table 1. The rightmost panel shows the innermost and highest resolution grid.

The calculations required 450 base level time-steps. This corresponds to ca 8,700 and 11,000 steps on the fourth and fifth level of refinement, respectively, for a total of 2×10^{13} MHD solver updates. The latter is the most expensive part of the code and the two finest levels is where most of the CPU cycles are used. Both the calculation and the data analysis required running on several thousand cores on a Cray XE6 at the Swiss National Supercomputing Center for a total cost of several hundreds of thousand of CPU hours.

3. RESULTS

The analysis below is restricted to data at redshift $z = 0$. The evolution of the presented results as a function of redshift will be presented elsewhere. We note however, that the simulated GC suffered a major merger around redshift 0.2, and has accumulated roughly half of its virial mass since then, 20% of which during the last $\frac{1}{2}$ Gyr. So it is currently in the process of strong dynamical relaxation.

3.1. Characterization of the Galaxy Cluster

We start with a description of the basic properties of the simulated GC. We run again our HOP halo finder to determine its center. We then determine various characteristic quantities including the virial radius enclosing a mass over-density $\Delta_c = 178 \Omega_m^{0.45}$ (Eke et al. 2001) with respect to the critical density, $R_{vir} = 1.95 h^{-1} \text{Mpc}$, and the corresponding enclosed mass, $M_{vir} = 1.27 \times 10^{15} M_{\odot}$. Other characteristic radii corresponding to higher over densities often used in the literature, include, $R_{200} \simeq 1.5 h^{-1} \text{Mpc}$, $R_{500} \simeq 1 h^{-1} \text{Mpc}$. The volume averaged gas temperature is 5.2 keV and the gas volume averaged rms velocity is 1927 km s^{-1} . These values are summarized in Table 2.

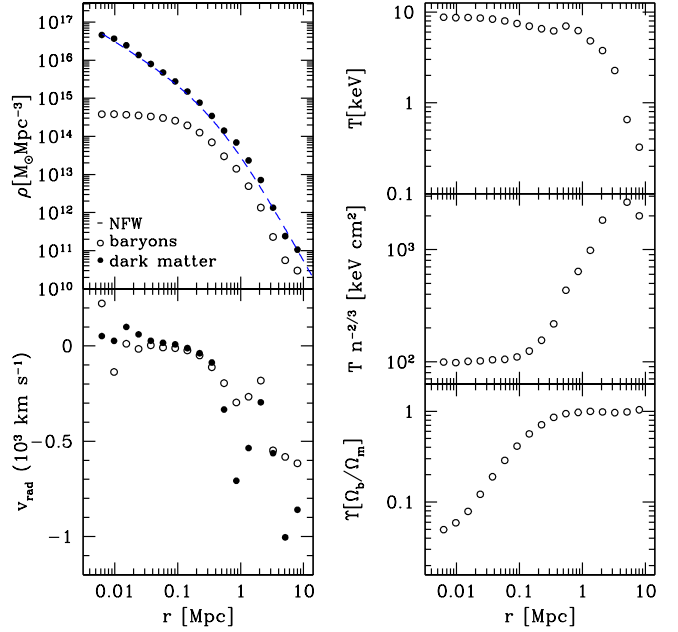


Figure 2. *Top Left:* Density profile of the baryonic gas (open circles) and dark matter (filled circles). The dash line correspond to a NFW profile with concentration parameter $c = 7.5$. *Bottom Left:* Profile of the radial velocity component for the baryonic (open circles) and dark matter (filled circles). The structure around 1 Mpc distance indicates the presence of a large infalling clump. *Top Right:* Gas temperature profile. The bump around 1 Mpc radial distance again is due to the presence of infalling clump. *Middle Right:* Volume averaged specific entropy radial profile. *Bottom Right:* Cumulative radial profile of the baryonic gas fraction, in units of the cosmic average value. The plots correspond to cosmological redshift $z = 0$.

3.1.1. Radial Profiles

In Figure 2 we show the radial profiles of additional basic quantities. The top left panel illustrates the density profiles for the baryonic gas (open circles) and dark matter component (filled circles), respectively. The dash line correspond to a NFW profile with concentration parameter $c = 7.5$. This is shown for illustration only, as no effort was made in fitting the precise value of this parameters, and we found that $c = 8$ also provides a viable choice to match the numerical profile. The plot shows the typical core distribution of the baryonic gas (open circles), where the average gas density is $n \simeq \text{a few } \times 10^{-2} \text{ cm}^{-3}$, versus the cuspy profile of the dark matter (filled circles). The bottom left panel shows the profile of the radial velocity component, again open circles for baryonic gas and filled circles for dark matter component, respectively. One can see velocity structure both in the inner region at radial distances around 10 kpc, and particularly a prominent feature around 1 Mpc. These are due to the presence of large infalling clumps. A feature around 1 Mpc, originating from the same event, is also visible in the temperature profile (top right panel). While volume average gas temperature is 5 keV, the baryonic gas in the GC core reaches hotter temperatures, around 9 keV, and stays relatively hot even beyond R_{vir} , with $T \sim 1 \text{ keV}$. The middle right panel shows the radial average entropy distribution. The radial profile rises steadily way beyond R_{200} and bends slightly only beyond the virial radius. It

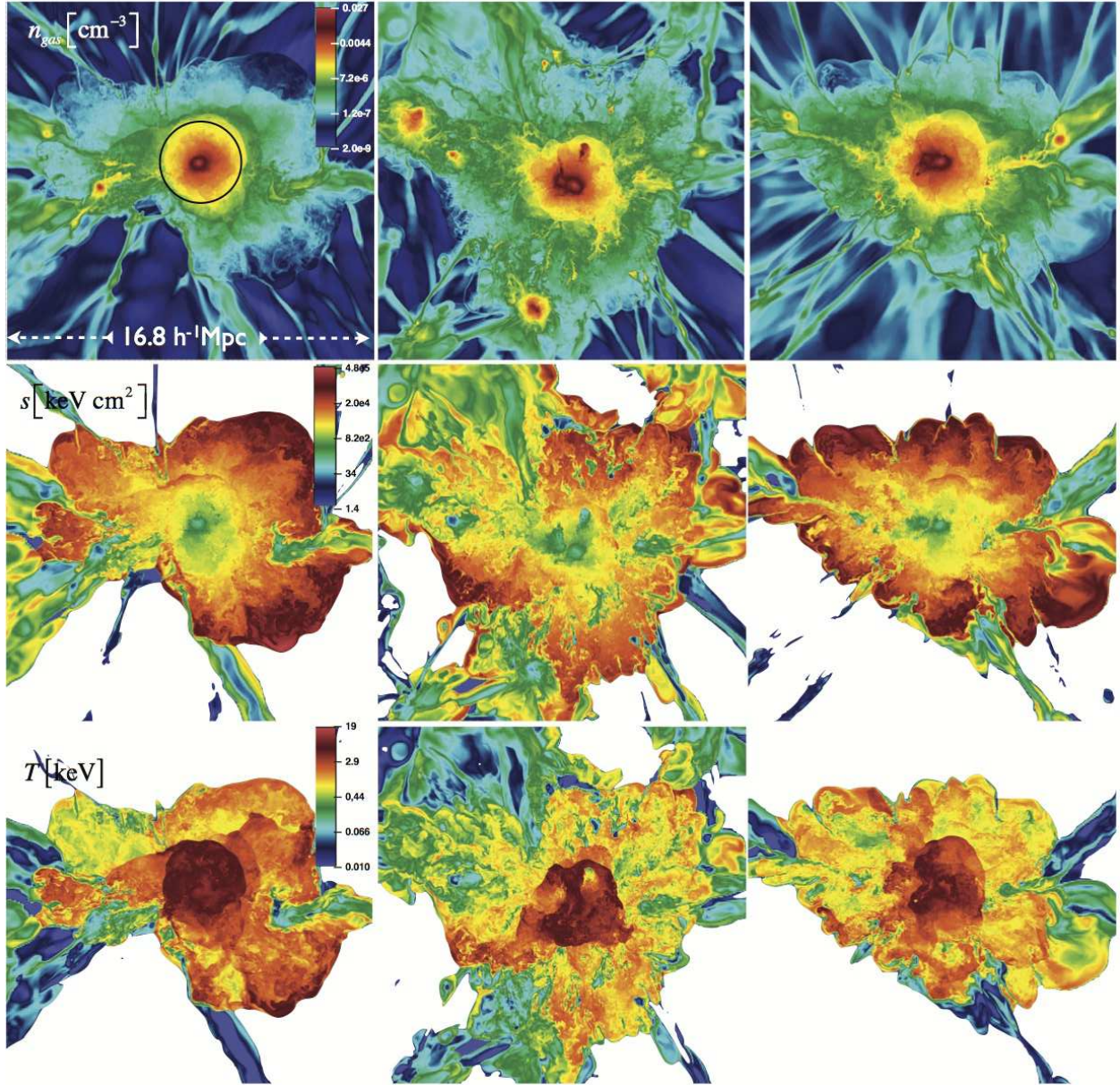


Figure 3. Two dimensional slices of density (top) gas specific entropy (second from top), and temperature (second from bottom), for three different planes passing through the GC center (left to right). Each panel is $16.8 h^{-1} \text{Mpc}$ on a side. The black circle in the top-left panel indicates the region enclosed within the virial radius. Color bar in physical units for each quantity is shown at the top-left corner of the leftmost panel.

turns over only at radii a few times R_{vir} , roughly the location of the external accretion shocks, beyond which the lay the intergalactic medium. Finally, the bottom right panel show the cumulative radial profile of the baryonic gas in units of the cosmic average value. In this simulation, the baryonic gas fraction reaches the cosmic average well within the virial radius.

3.1.2. Two-dimensional Maps

Figure 3 shows two dimensional slices of density (top), gas specific entropy (middle), and temperature (bottom), respectively, for three different planes passing through the GC center (left to right). The size of the panel on a side is about $16.8 h^{-1} \text{Mpc}$. The center of the GC is roughly located at the density peak in the top panels. The region enclosed within virial radius, R_{vir} , is illus-

trated by the black circle.

The first point to notice is that, as illustrated by Figure 3, the virial volume of the GC is embedded in a much larger volume filled with hot gas and enveloped by the external accretion shocks at a few times the virial radius. We refer to the gas hot within the external accretion shocks, including the hot gas beyond the virial radius, i.e. formally outside the GC volume, still as the ICM. The external accretion shocks, where the temperature jumps from sub eV to keV temperatures, are found 2-3 R_{vir} from the GC center. This is much further out than the virial radius, as well as the radius R_{200} ($\sim 3/4 R_{\text{vir}}$), which X-ray observations are now starting to explore.

From the morphological perspective, the overall shape of the ICM in Figure 3 appears very irregular. The maps on the left panel are strongly asymmetric, the one on

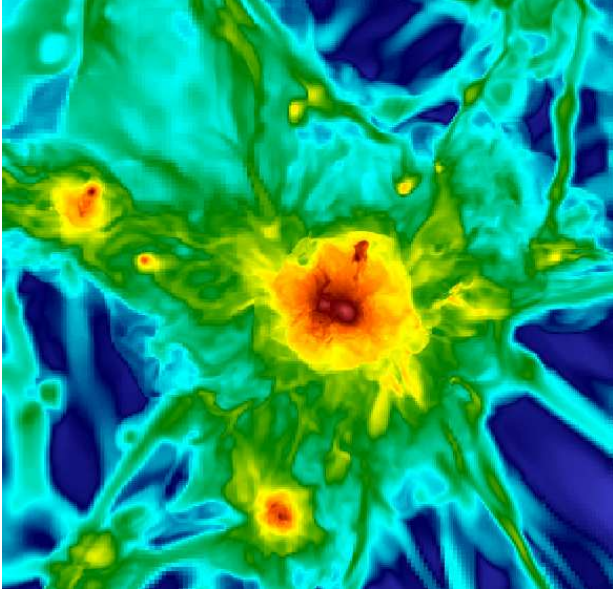


Figure 4. Two dimensional slices of density, just as in the central top panel of Fig. 3, but from an AMR simulation based on Lagrangian refinement criterion.

the right elongated, the one in the center very extended. The surface of the accretion shocks also appear highly structured and irregular. Large scale asymmetries are revealed by maps of various thermodynamic quantities which appear quite different on different planes. In the following Section we will describe the role of these large scale irregularities, including the shock surface structures, in generating turbulence. Perhaps the most striking features is the tremendous amount of structure exhibited in the maps, particularly in the GC outskirts. This is due to fluid instabilities and turbulent motions. Their development is made possible by the relatively high Re number allowed by the uniform high numerical resolution across the GC volume. For comparison, in Figure 4 we show the same density map as shown in the top central panel of Figure 3, but obtained with a simulation which is identical in all respects to the one being presented here, e.g. in terms of initial conditions, cosmological parameters, max spatial resolution etc., except that it employs adaptive mesh refinement based on Lagrangian criterion. Specifically grid cells are tagged for refinement when their mass content is eight times as large as the mean comoving value. Simple visual inspection shows that while the two simulations are fully consistent with each other in terms of gross flow features, in the Lagrangian AMR case one does not see fine structure of the flow as fluid instabilities hardly develop on small scales. A more quantitative analysis based on velocity structure functions is presented in Section 3.4.2.

The small and large scale fluid structure in the maps of Figure 3 is due to the fact that the system is dynamically active, i.e. is still forming. Specific entropy traces the thermal history of a fluid element due to non-adiabatic processes. Lacking any endothermic and/or exothermic processes, the only non-adiabatic processes here are those due to shock heating. The specific entropy maps allows us to recognize the presence of clumps tracing merging substructures that are floating around the GC potential, and filaments, in addition to the GC core.

All of them have formed relatively early. The gas in the clumps and filaments, subject to various fluid instabilities such as Rayleigh-Taylor, Kelvin-Helmholtz, turbulent drag, is stripped and deposited in the ICM. Mixing with the ICM is, however, incomplete. The motion of the substructures traced by low entropy gas is particularly important in generating turbulence in the ICM. The temperature maps (second from bottom) show also large inhomogeneities. These are partly due to the presence of gas with different thermal history as discussed above, which include the clumps but also the large filament in the leftmost panel. Another important source of temperature structure is the presence of large scale shocks, extending across a large fraction of the GC volume. These internal shocks play an important role in the generation of turbulence, which is discussed in the next section.

The properties of the turbulent flow across the GC vary with radial distance. For this reason in the following we typically distinguish four different radial regions in which we carry out the analysis. These are defined as: *core* with $R < \frac{1}{3}R_{\text{vir}}$, *off-core* with $\frac{1}{3}R_{\text{vir}} < R < \frac{2}{3}R_{\text{vir}}$, *virial* with $\frac{2}{3}R_{\text{vir}} < R < R_{\text{vir}}$, and, *off-virial* with $R_{\text{vir}} < R < \frac{4}{3}R_{\text{vir}}$.

3.2. Turbulence Injection Mechanisms

In view of the analysis presented below, it is useful to discuss the various processes that contribute to the generation of the turbulence in the ICM. Turbulence is generated by shearing flows and the baroclinic term. Shearing flows are unstable to turbulence when the Reynolds number is sufficiently large. On the other hand the baroclinic term generates vorticity, $\boldsymbol{\omega} \equiv \nabla \times \mathbf{v}$, according to (Landau & Lifshitz 1987),

$$\frac{\partial \boldsymbol{\omega}}{\partial t} = \nabla \times (\mathbf{v} \times \boldsymbol{\omega}) + \nabla P \times \nabla \frac{1}{\rho}, \quad (1)$$

which in turn excites turbulence. The baroclinic term appears when the fluid pressure depends explicitly on both density and temperature, $p = p(\rho, T)$, i.e. the fluid is baroclinic. Shocks are a strong source of baroclinicity but, as shown below, not the only one. Both shear flows and the baroclinic term can be traced back to

1. tidal fields
2. merging substructure

with gravity the ultimate source of energy.

Due to the presence of tidal fields in the volume around the GC, the velocity field of the accretion flow is anisotropic, and the accretion shocks acquire an irregular shape. This is important for two reasons. Firstly, as a result of the changing curvature of the shock surface, vorticity is generated by the baroclinic term. Secondly, the accretion shocks have an *oblique* character, i.e. they are quite inefficient at dissipating the upstream flow kinetic energy (Miniati et al. 2000). Downstream the accretion shocks residual trans and supersonic motions persist, and the gas temperature remains modest (~ 1 keV). The interaction of these residual motions generates turbulent cascades, as well as large scale shocks internal to the ICM, particularly in the region around and beyond the virial radius. The internal shocks in turn generate vorticity through the baroclinic term, which is particularly

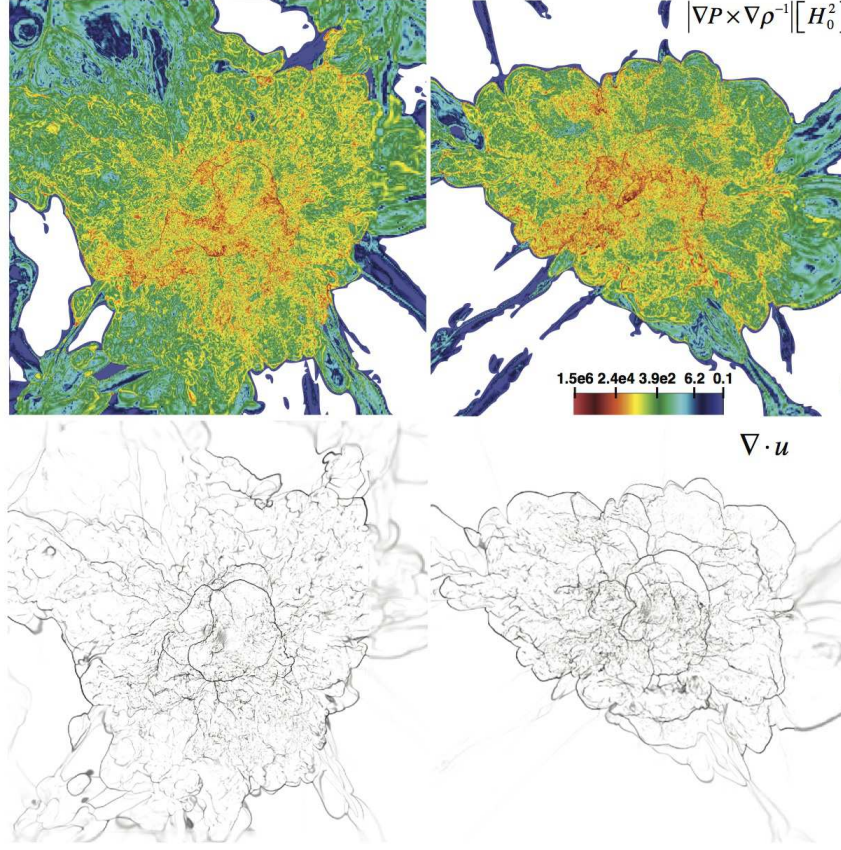


Figure 5. Two dimensional slices of baroclinic term's magnitude (top) and velocity divergence (bottom), for two different planes passing through the GC center (left to right). Each panel is $16.8 h^{-1} \text{Mpc}$ on a side. Color bar for the baroclinic plot is shown in the top-right panel in physical units of H_0^2 .

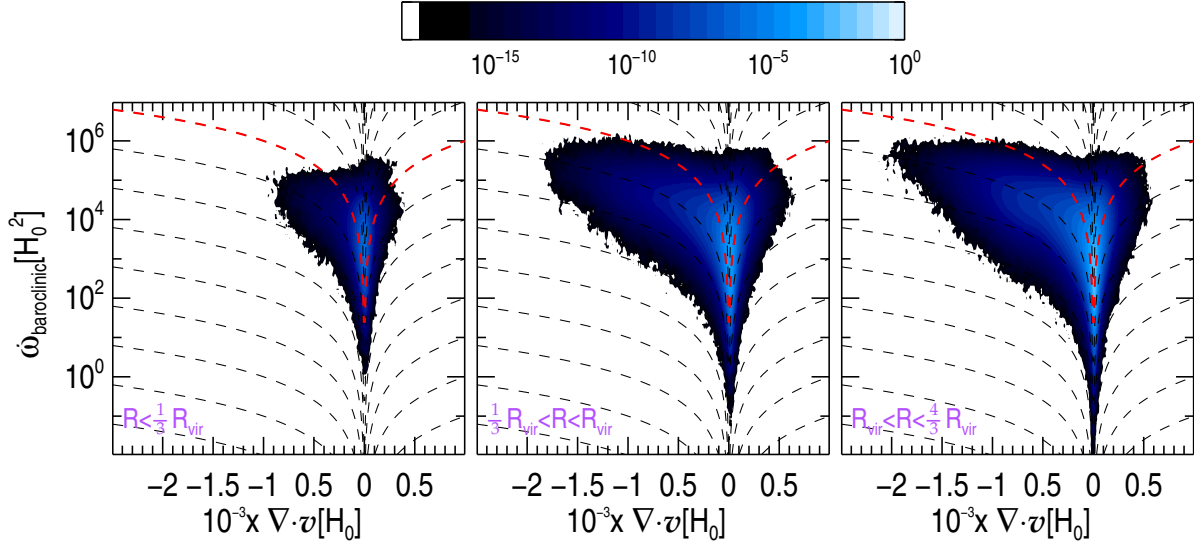


Figure 6. Phase-space diagram of the baroclinic term's magnitude ($\dot{\omega}_{\text{baroclinic}}$) in units of H_0^2 versus velocity divergence in units $10^3 H_0$. The three panels correspond to the core region (left), the off-core and virial region (center), and the off-virial region (right). The dash diagonal lines are loci where $\dot{\omega}_{\text{baroclinic}} = A(\nabla \cdot v)^2$, with A given by the label in the leftmost panel. The red line corresponds to $A = 1$. For lines below and above it, the factor A is progressively smaller and larger by a factor 10, respectively.

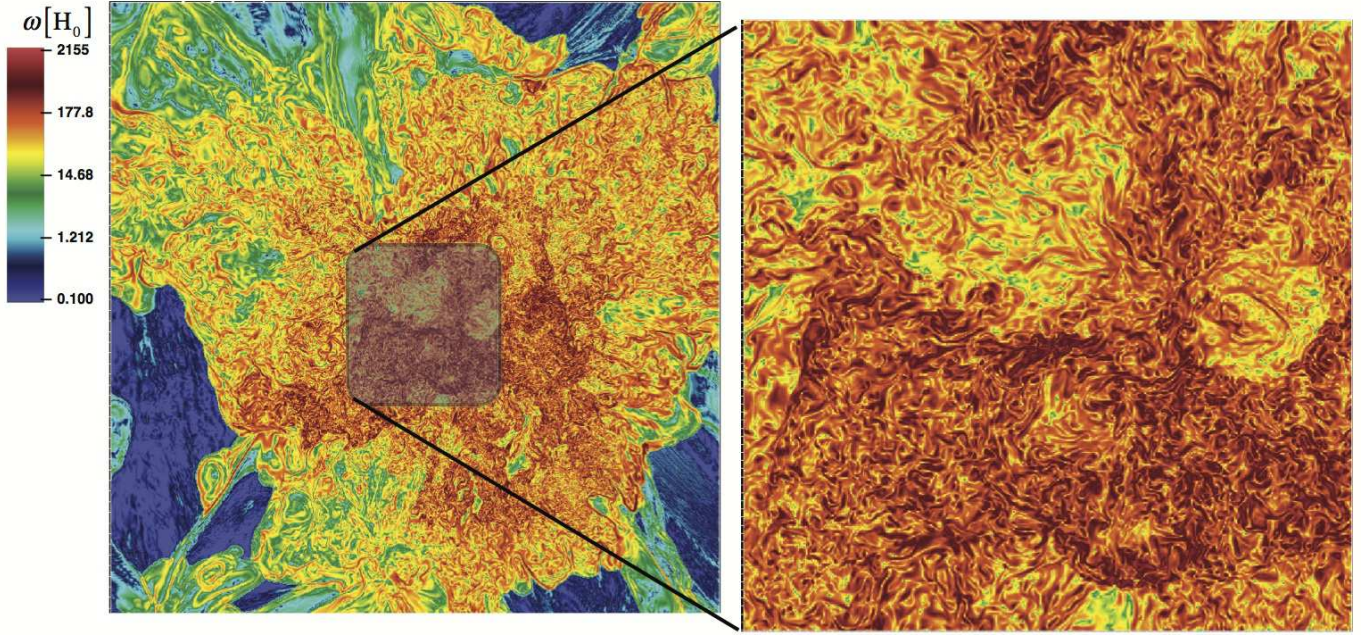


Figure 7. *Left:* Two dimensional slice of vorticity magnitude on a plane passing through the GC center. The plane orientation is as in the middle panels of Figure 3. *Right:* Zoom-in of the shaded area in the left panel. Vorticity is expressed in units of the Hubble's constant, with color-bar on the top-left of the figure.

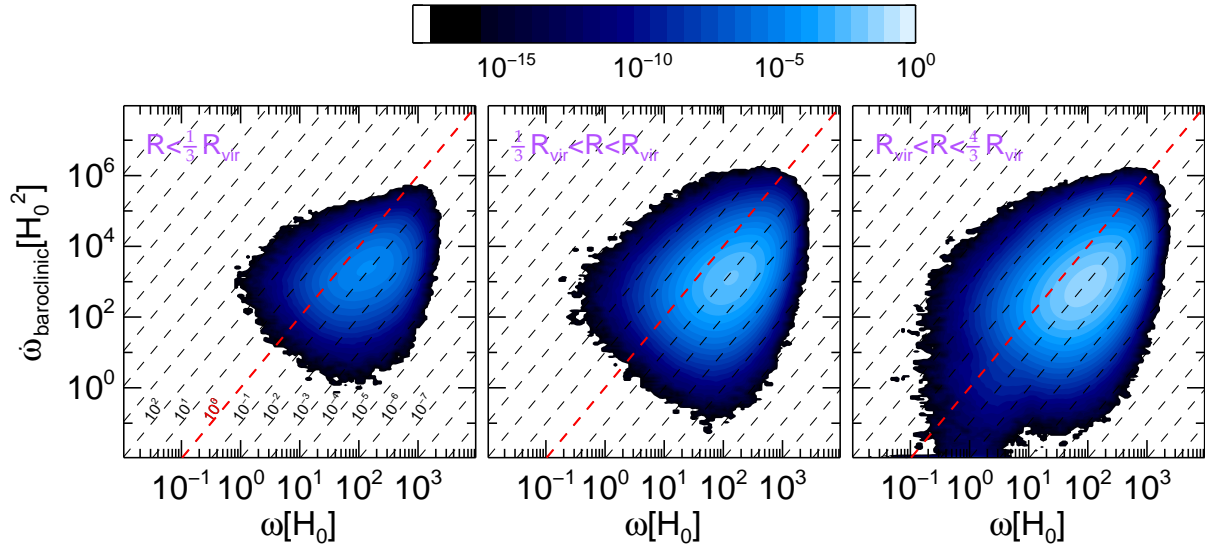


Figure 8. Phase-space diagram of the baroclinic term's magnitude ($\dot{\omega}_{\text{baroclinic}}$) in units of H_0^2 versus vorticity in units H_0 . The three panels correspond to the core region (left), the off-core and virial region (center), and the off-virial region (right). The dash diagonal lines are loci where $\dot{\omega}_{\text{baroclinic}} = A\omega^2$, with A given by the label in the leftmost panel, and with the red line corresponding to $A = 1$.

strong at sites of shock-shock collisions. These shocks, therefore, further contribute to the generation of turbulence.

The top panels of Figure 5 shows two dimensional maps of the baroclinic term for two different planes passing through the GC center (the same planes in the central and right panels of Fig. 3). The two bottom panels illustrate the position of the shocks in the same planes through the negative divergence of the velocity. The figure shows that the ICM is pervaded by a fine network of predominantly weak shocks. These shocks generate a baroclinic term all over the ICM, with the strength of the latter depending on the strength of the former. However, the baroclinic term appears more volume filling than shocks. This reveals that shocks are not the only source of baroclinicity. This is better illustrated in Figure 6, which presents the phase-space diagram of the baroclinic term versus velocity divergence. The three panels correspond to the core (left), off-core + virial (center), and off-virial (right) region, respectively. Clearly the baroclinic term is active not only in regions of negative velocity divergence (shocks), but also in regions where the latter quantity is null or positive, i.e. without shocks. In fact, due to the hierarchical assembly of a GC, the ICM is composed of mixtures of gas with different thermodynamic histories. In particular, there coexist polytropic gas with different entropy. This implies that the ICM deviates significantly from a barotropic fluid, i.e. is generally baroclinic, and generation of vorticity does not necessarily require shocks. In fact, in the specific case illustrated here, shocks generate baroclinicity in 60% of the cases in the core region, but only 40% everywhere else (out to the off-virial region). This may sound counter-intuitive, but is related to the fact that while the gas in the outskirts regions is more compressional, shocks there are not as pervasive as in the GC inner regions (see Figure 5).

The spatial scale characterizing the gradient of the velocity field associated to the accretion and the residual post-shock flows can be estimated of order the curvature radius of the external and internal shocks, which in turn is of order the virial radius, i.e. $L \sim R_{\text{vir}}$. The velocity field can be estimated using the scaling relation, yielding, $v_{\text{vir}} = \sqrt{GM_{\text{vir}}/R_{\text{vir}}}$. Therefore, the characteristic rate associated to the turbulent cascade is the dynamical timescale of a virialized structure,

$$\tau_{\text{turb}}^{-1}(z) \simeq \frac{v_{\text{vir}}}{R_{\text{vir}}} \sim \Delta_c^{\frac{1}{2}} H(z) \gg H(z), \quad (2)$$

and is fast compared to the cosmological timescale. Note that this statement is true for collapsed halos regardless of redshift.

Merging halos and substructures floating through the GC potential, also contribute to stirring up energetic motions in the ICM. In particular, turbulence is generated in the wakes of these halos as they move through the ICM (Subramanian et al. 2006). The injection scale is around the halo ram pressure stripping radius. The volume filling factor is very sensitive to the Reynolds number, which determines the length of the wake (Subramanian et al. 2006). Only during major mergers, i.e. mergers with structures of similar mass, is turbulence injected on large scales, $L \lesssim R_{\text{vir}}$, and with

large volume filling factor. For most substructure, the injection scale is considerably smaller, i.e. $L \sim 100$ kpc, for a sub-halo mass $m \simeq 10^{13} M_{\odot}$. The filling factor is uncertain due to the unknown viscosity of the ICM, but remains small compared to unity if viscosity is provided by Coulomb collisions. In addition to the turbulent wakes, moving substructure generate bow shocks which are weak during core passage, but steepen as they enter the low density regions at and beyond the virial radius. These shocks generate vorticity and, hence, turbulence as discussed above. The injection scale can be estimated a few times the characteristic size of the halo, which is given by the above ram pressure stripping radius, i.e. $L \sim \text{a few} \times 100$ kpc.

Because in general $L \lesssim R_{\text{vir}}$, and the velocity involved is of order v_{vir} , the conditions expressed by Eq. (2) remain valid, i.e. there is sufficient time for the motions generated by mergers and moving substructures to generate a turbulent cascade during a Hubble time at virtually any redshift.

Finally, the filaments through which the merging halos accrete onto GC, provide another example of anisotropic accretion and source of turbulence. Filaments of different sizes penetrate through the GC atmosphere, with the largest filaments reaching the core region. The strong shear flow that is present at the ICM-filament interface is subject to Kelvin-Helmholtz instability. Inspection of Figure 3 shows that filaments inside the ICM are indeed unstable, with the small sized ones being completely disrupted. The instability extracts the free energy of the gas in the filaments and feeds turbulence. Additionally, large filaments typically terminate with a shock, which is a source of additional turbulence as discussed above. Filaments come in different sizes, but the characteristic length, L , scales for the injection of turbulence by the instability and by the filament termination shocks are of the same order as discussed above for the substructure. Therefore, Eq. (2) applies as well in this case.

In conclusion, large scale motions appear to be generated on a range of spatial scales by different processes. The largest scales reach up to R_{vir} , or a fraction thereof, and are contributed by tidal fields and major mergers. Smaller structure stirs fluid motions on accordingly smaller scales. In any case, the characteristic time L/v is in general much smaller than the Hubble time.

3.3. Signatures of Fully Developed Turbulence

The panel on the left hand side of Figure 7 shows the distribution of the vorticity in a plane passing through the GC center. The plane orientation is as in the middle panels of Figure 7, although the distribution of vorticity on different planes is quite similar. The panel on the right hand side is a zoom in of the shaded area in the central region of the left panel. The vorticity is evaluated on scales $\ell = 2\Delta x_5 = 14.6 h^{-1}$ kpc, corresponding to the finest grid, with a cell-centered finite difference scheme, and is expressed in units of H_0 .

Figure 7 shows that inside the accretion shocks the value of the vorticity is quite high, ranging from a few tens (yellow) to a few thousand (red). This is consistent with results in, e.g., Ryu et al. (2008) and Zhu et al. (2011). Since vorticity is expressed in units of H_0 , this means that vortical motions are fully developed on scales of a few tens of kpc. The right panel of Figure 7 shows

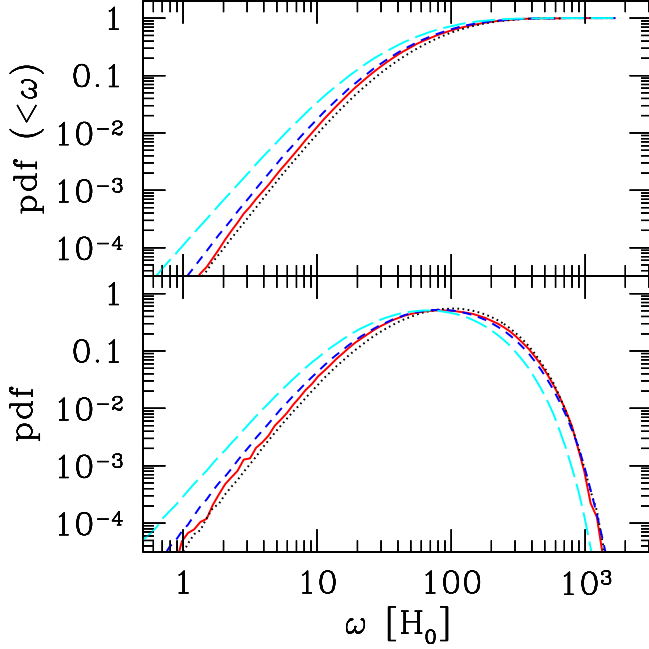


Figure 9. Cumulative (top) and ordinary (bottom) probability density function of the vorticity per Log vorticity interval. Vorticity is computed on a scale twice the mesh size of the finest grid, i.e. $\ell = 2\Delta x_5 = 14.6 h^{-1}$ kpc. Different lines from left to right correspond to the following regions: off-virial for $R_{\text{vir}} < R < \frac{4}{3}R_{\text{vir}}$ (long-dash cyan), virial radius for $\frac{2}{3}R_{\text{vir}} < R < R_{\text{vir}}$ (short-dash blue), off-core for $\frac{1}{3}R_{\text{vir}} < R < \frac{2}{3}R_{\text{vir}}$ (dot black), core for $R < \frac{1}{3}R_{\text{vir}}$ (solid red). Note how dot and solid lines are nearly indistinguishable.

more clearly that the vorticity developed very fine structure, all the way down to the finest scales allowed by the mesh size of the grid.

Figure 8 presents a baroclinic term versus vorticity phase-space diagram. The three panels from left to right correspond to the core, off-core + virial, and off-virial regions, respectively. The peak value of both vorticity and baroclinic term become stronger in the outer regions of the cluster, in agreement with Figure 5 and 7. In addition, this figure also shows a weak correlation between the two quantities. Namely the baroclinic term appears roughly proportional to the square of the vorticity, a relation followed by oblique dash lines (with the thick (red) line corresponding to unit proportionality constant). Most of the vorticity lives in a region of phase space where the constant of proportionality is between 1 and 10^{-2} . This is suggestive that the vorticity develops on a time scale roughly between 1-100 times its inverse. A similar qualitative conclusion can be inferred by the analysis of the dashed lines in Figure 3, which correspond to curves $\dot{\omega}_{\text{baroclinic}} \propto (\nabla \cdot \mathbf{v})^2$, if we replace the vorticity with the velocity divergence.

The top panel of Figure 9 shows the cumulative probability density function (pdf) of the vorticity per log vorticity interval. Different curves correspond to different spherical shells around the GC, i.e. core (solid-red line), off-core (dotted-black line), virial (short-dashed-blue line), and finally, off-virial (long-dashed-cyan line). The three pdf's within the virial radius (solid, dot and short-dash lines) are almost indistinguishable while the peak of the long-dashed line (off-virial) is shifted to the

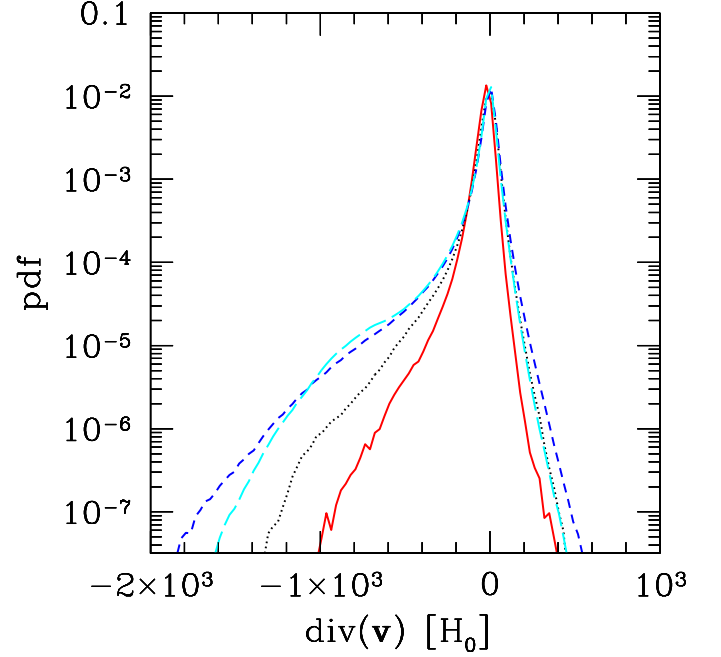


Figure 10. Probability distribution function of the velocity divergence. Line style and color is the same as in Figure 9.

left by a factor $\lesssim 2$ compared to solid line (core), suggesting a slight trend for the vorticity to become slower, on average, towards the outer regions. In comparison, inspection of Figure 9 indicates that the vorticity outside the accretion shocks is much lower and is narrowly distributed around values a few times $0.1 H_0$. In any case, the pdf's in Figure 9 confirm the visual impression provided by the two-dimensional slice that high vorticity is characterized by a quite large volume filling factor. For example, 99% of space inside the virial volume has vorticity $\omega > 10 H_0$. Outside the virial radius, that percentage drops only slightly to 96%. The high filling factor of the vorticity found here is in contrast with the results in Iapichino & Niemeyer (2008), most likely because the GC studied by those authors was a relatively relaxed system.

Since the numerical viscosity acts on scales larger than the actual collisional mean free path, the Reynolds number of the simulated flow is not sufficient to ensure high filling factor of the turbulent wakes generated by moving galactic substructure (Subramanian et al. 2006). Therefore, this suggests that most of the vorticity inside the ICM is generated by shocks and filaments.

If we assume Kolmogorov scaling for the vorticity, $\omega_\ell \propto v_\ell/\ell \propto \ell^{-2/3}$, we can estimate the pdf of the vorticity also on larger scales by shifting accordingly the x-axis of Figure 9, i.e. by a factor $(10^3/14.6)^{2/3} \simeq 26$ for scales comparable to the injection scale. We then conclude that even on the largest scales where we expect shear flows to be generated, the vortical motions remain fast compared to the Hubble time, for a significant fraction of the GC volume and at different distances from the GC center.

The bottom panel of Figure 9 shows the (non-cumulative) vorticity pdf per log interval. We find that each pdf can be very well approximated by function of

Table 3
pdf's Fit Parameters

Region	$\bar{\omega}$ (H_0)	σ_ω (H_0)
core	14	240
off-core	16.5	240
virial	12	240
off-virial	9	185

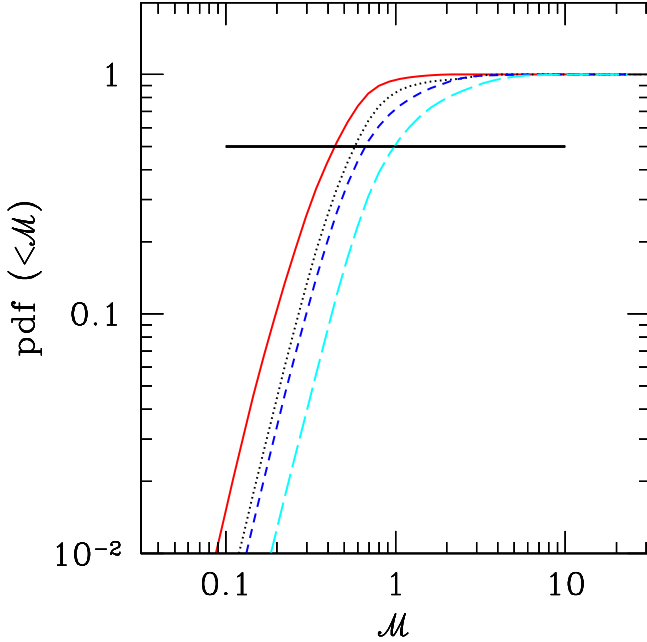


Figure 11. Cumulative probability distribution function of the flow Mach number for different regions around the GC center. Line style and color is the same as in Figure 9. The horizontal line corresponds to the value $\frac{1}{2}$, intersecting each pdf at the median value.

the form

$$\text{pdf} = A \frac{\omega^3}{\omega^2 + \bar{\omega}^2} e^{-\frac{|\omega - \bar{\omega}|}{\sigma_\omega}}, \quad (3)$$

where, $\bar{\omega}$ and σ_ω are fitting parameters but can be identified as is the peak value and the width of the distribution, respectively, while A is a normalization factor. Fitting parameters for the various curves are reported in Table 3. In particular, for large values of the vorticity, $\omega > \bar{\omega}$, the pdf's exhibit an exponential cutoff. This feature is characteristic of fully developed compressible turbulence with modest Mach number, as demonstrated in the numerical simulations in Porter et al. (2002).

The same features characteristic of fully developed compressible turbulence appear in the pdf of the velocity divergence presented in Figure 10. Different curves are style and color coded as in Figure 9. In particular, the strong asymmetry of the pdf and the extended wings towards negative value of the divergence with almost power-law shape, is associated to the presence of numerous shocks and resemble qualitatively those reported in Porter et al. (2002) and Schmidt et al. (2009).

Finally, in Figure 11 we plot the cumulative pdf of

the Mach number, $\mathcal{M} \equiv u/c_s$, with c_s the gas sound speed. As in the previous figures, the four curves in Figure 11 correspond to the four regions around the GC center, from the core (leftmost, solid red curve) to the off-virial region (rightmost, long-dash cyan curve). Since the gas is not isothermal, with a general trend of the temperature to decrease towards the outer regions (see Figure 2), the Mach number is a function of both the fluid element velocity and local temperature. The intersection of the pdf with the solid horizontal line marks the median Mach number of the pdf. In fact, the cumulative pdf's in Figure 11 become broader towards the outer region, indicating that the flow is progressively more compressible. The higher level of turbulent energy found in the low density intergalactic medium compared to the ICM by Iapichino et al. (2011) is probably related to this effect. In the core region, the Mach number is mostly between 0.1-1, with a median value of $\lesssim 0.5$, indicating that the gas is mildly compressible. Moving outward in space the gas compressibility increases, with the median Mach number taking the values 0.6 (off-core), 0.7 (virial) and ~ 1 off-virial.

In conclusion, the analysis carried out in this section indicates that both in the core and in the distant outskirts the vorticity is volume filling and with a timescale short compare to the Hubble time even on scales comparable to R_{vir} . In addition, the pdf of the vorticity and the velocity divergence are qualitatively very similar to those observed in simulations of compressible turbulence with comparable Mach numbers to those characterizing our simulated flows. The median Mach number is typically less than one, ranging from 0.5 to 1 from the core to the off-virial regions, respectively. Consistent with expectations based on the analysis in Sec. 3.2, the ICM appears in a state of fully developed turbulence. This conclusion is further corroborated by results in the next section.

3.4. Structure Functions

In this section we study the statistical properties of the velocity increments as a function of spatial separation. This is carried out by computing the structure functions of order p , for both the longitudinal and transverse components of the velocity field. In addition, the velocity field is decomposed into the solenoidal, \mathbf{v}_s , and potential or compressional, \mathbf{v}_c , components using the Hodge-Helmholtz decomposition, i.e.

$$\mathbf{v} = \mathbf{v}_s + \mathbf{v}_c, \quad (4)$$

$$\mathbf{v}_c = -\nabla\phi, \quad \mathbf{v}_s = \nabla \times \mathbf{A}, \quad (5)$$

$$\phi = \frac{1}{4\pi} \int \frac{\nabla \cdot \mathbf{v}}{r} d\mathbf{x}, \quad \mathbf{A} = \frac{1}{4\pi} \int \frac{\nabla \times \mathbf{v}}{r} d\mathbf{x}. \quad (6)$$

The longitudinal and transverse structure functions of order p are then computed for each velocity component as

$$\langle \delta v_{\ell}^p \rangle_{l,q} = \langle |[\mathbf{v}_q(\mathbf{x} + \ell \mathbf{n}) - \mathbf{v}_q(\mathbf{x})] \cdot \mathbf{n}|^p \rangle, \quad (7)$$

$$\langle \delta v_{\ell}^p \rangle_{t,q} = \langle |[\mathbf{v}_q(\mathbf{x} + \ell \mathbf{n}) - \mathbf{v}_q(\mathbf{x})] \cdot \mathbf{t}|^p \rangle, \quad (8)$$

where ℓ is the spatial separation and \mathbf{n} , \mathbf{t} are a unit directional vector, with $\mathbf{t} \equiv (\mathbf{n} \times (\mathbf{v}_q \times \mathbf{n})) / |\mathbf{v}_q|$, while $q = c, s$, refers to the solenoidal and compressional components, respectively.

Table 4
Turbulence Results

Region	solenoidal						compressional					
	$L_{\text{inj}}^{\parallel}$ (R_{vir})	ζ_2^{\parallel}	ζ_3^{\parallel}	L_{inj}^{\perp} (R_{vir})	ζ_2^{\perp}	ζ_3^{\perp}	$L_{\text{inj}}^{\parallel}$ (R_{vir})	ζ_2^{\parallel}	ζ_3^{\parallel}	L_{inj}^{\perp} (R_{vir})	ζ_2^{\perp}	ζ_3^{\perp}
core	≈ 0.7	0.80	1.15	≈ 0.6	0.69	0.97	≈ 0.9	1.16	1.56	≈ 0.8	1.24	1.61
off-core	≈ 1.0	0.67	0.95	≈ 0.8	0.64	0.91	≈ 1.0	0.97	1.20	≈ 0.8	1.10	1.30
virial	≈ 1.5	0.60	0.82	≈ 1.0	0.58	0.78	≈ 1.0	0.77	0.82	≈ 0.9	1.06	1.17
off-virial	> 1.5	0.66	0.91	≈ 1.2	0.61	0.83	> 1.5	0.85	0.95	> 1.5	0.98	1.05

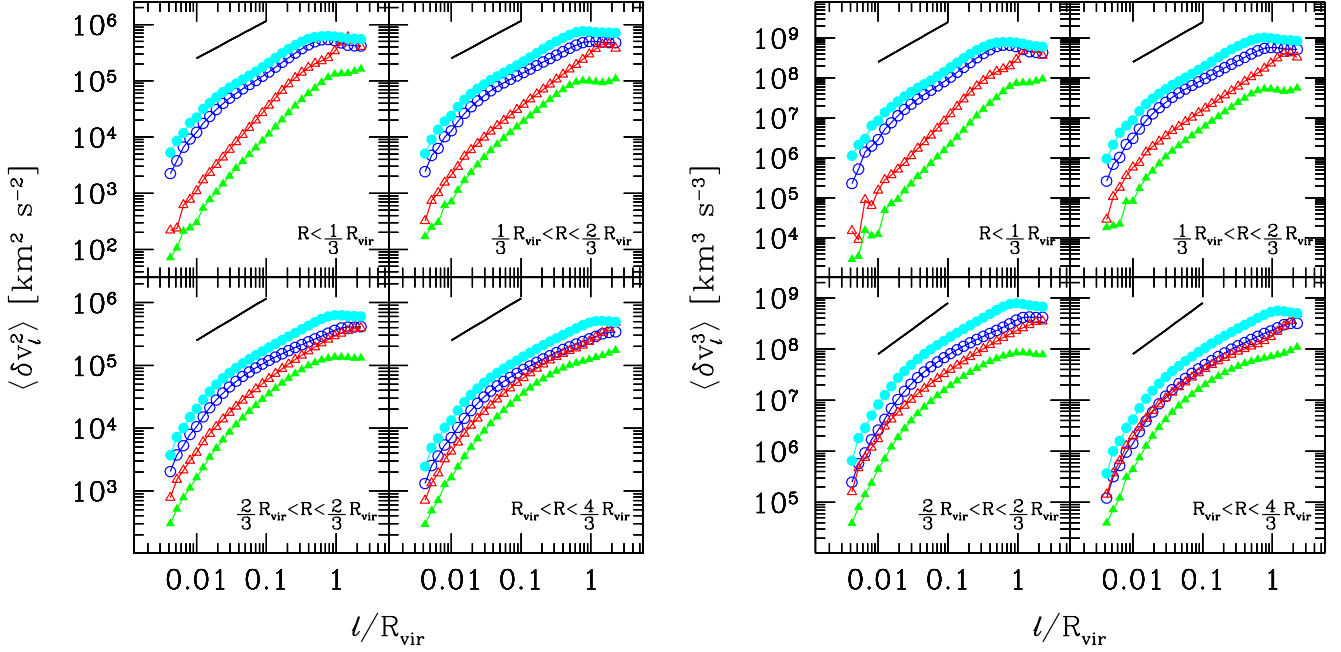


Figure 12. Second (left) and third (right) order structure function of the velocity field. Different curves from top to bottom correspond to the following components: solenoidal–longitudinal (blue open circles), solenoidal–transverse (cyan solid circles), compressible–longitudinal (red open triangles), compressible–transverse (green solid triangles). The structure functions in the different panels were sampled from different shell volumes centered around the GC center, namely: core corresponding to $R < (1/3)R_{\text{vir}}$ (top left), off-core corresponding to $(1/3)R_{\text{vir}} < R < (2/3)R_{\text{vir}}$ (top right), virial corresponding to $(2/3)R_{\text{vir}} < R < R_{\text{vir}}$ (bottom left), off-virial corresponding to $R_{\text{vir}} < R < (4/3)R_{\text{vir}}$ (bottom right).

In Figure 12 we present second (left) and third order (right) velocity structure functions for the different velocity components discussed above and extracted from different sub-volumes of the GC. In particular, curves from top to bottom correspond to solenoidal-transverse (cyan circles), solenoidal-longitudinal (blue circles), compressible-transverse (red triangles) and compressible-longitudinal (green triangles) components, respectively. In addition, the different panels correspond to the core (top left), off-core (top right), virial (bottom left), and off-virial (bottom right) region, respectively. Finally, for reference, the black line shows the prediction for fully developed incompressible, isotropic and homogeneous turbulence (Kolmogorov 1941a,b; Oboukhov 1941, hereafter K41). To compute the structure function we define sampling points randomly distributed inside the volume of interest and compute the velocity difference with respect to randomly selected field points at a maximum distances of $2 R_{\text{vir}}$. A total of $\lesssim 10^6$ sampling points and $\lesssim 10^6$ field points are used for the purpose, assigned to each sub-region proportionally to volume.

A number of important features characterize the structure functions in Figure 12. On scales $\ell \lesssim \alpha_l R_{\text{vir}}$, with $\alpha_l \sim 3 - 4 \times 10^{-2}$, corresponding to $\ell \simeq 10 \times \Delta x \simeq 100$ kpc, the structure functions generally steeper, due to the

influence of numerical dissipation as discussed in Sec. 2.2. At separation scales $\ell \gtrsim \alpha_h R_{\text{vir}}$, with $\alpha_h \sim 1$ the velocity increments are no more correlated and the structure functions tend to flatten out, although non-zero slope is noticeable most likely as a result of spatial inhomogeneity. The scale $\alpha_h R_{\text{vir}}$ grossly defines the curvature radius of the accretion and internal shocks, as well as the large scale shear flows, as discussed in Sec. 3.2. Furthermore, as discussed in Sec. 3.3, the timescale associated to vortical motions at this scale are short compared to the Hubble time. Therefore this is most likely the injection scale of the turbulence, whereas the scale interval $\alpha_l \lesssim \ell/R_{\text{vir}} \lesssim \alpha_h$, where both the second and third order structure functions exhibit power-law scale free behavior, $\langle \delta v_\ell^p \rangle \propto \ell^{\zeta_p}$, is identified as the inertial range of the turbulent cascade. For comparison, a similar value for the injection scale was found by Vazza et al. (2011) who computed the third order structure function, averaged over a sample of clusters, for the total velocity ($\mathbf{v}_s + \mathbf{v}_c$) and the whole GC volume, without longitudinal or transverse projection (see also Valdarnini 2011, for density weighted structure functions in the core region).

The properties of the structure functions reported in Figure 12, including the injection scales and the slopes in the inertial range, are summarized in Table 4. These

numbers should not be taken as precise “measurements”, because occasionally the structure functions themselves are not perfect power laws even in the inertial range. In addition, the condition of the ICM are changeable, so the values determined at this particular time and for this particular system will be different for different times and systems. However, the qualitative properties reflected in the reported value have probably general character and are discussed below. Similarly, the value of the velocity increments at given separation scales can be compared to the sound speed as inferred from the temperature profile provided in Figure 2, to check for departure from conditions of hydrostatic equilibrium. The same cautionary note, however, applies here.

For both the solenoidal and compressional components the injection scale of the turbulence appears to increase towards the GC outer region, ranging from $\gtrsim 0.7 R_{\text{vir}}$ in the core to the $\gtrsim R_{\text{vir}}$ around the virial region. Note that, particularly in the outer GC regions, the longitudinal structure functions do not flatten as much as the transverse component. This is likely due to the fact that as we approach the virial region, we start to sample velocity differences with respect to gas outside the external accretion shocks, where the flows is laminar. As for the solenoidal component, the spectral slope in the inertial range is close to the value predicted by Kolmogorov’s theory for incompressible, homogeneous and isotropic turbulence (Kolmogorov 1941a,b; Oboukhov 1941), despite the strong departures from the assumptions in that theory. This is in agreement with previous work on compressible turbulence with moderate to large Mach numbers (Porter et al. 1992, 2002; Kritsuk et al. 2007). Note that the spectral slopes become slightly flatter towards the outskirts region of the GC. This is related to the corresponding increase in the turbulence driving scale mentioned above and is discussed further below. The spectral slopes of the structure functions for the compressible components (open and solid triangles), are significantly steeper than in the solenoidal case, particularly in the core region, and actually roughly consistent with Burgers’ model of turbulence (Burgers 1939). Note, however, that as for the solenoidal case the compressible structure functions also tend to become flatter towards the outer region of the GC.

For incompressible, isotropic and homogeneous turbulent flow, an analytic relation exists between the transverse and longitudinal second order structure functions (de Karman & Howarth 1938; Landau & Lifshitz 1987), i.e.

$$\langle \delta v_\ell^2 \rangle_{t,s} = \frac{2 + \zeta_2}{2} \langle \delta v_\ell^2 \rangle_{l,s} \approx \frac{4}{3} \langle \delta v_\ell^2 \rangle_{l,s} \quad (9)$$

where the last approximation assumes close to K41 scaling. This relation holds to a good approximation even for compressional flows, as demonstrated in Kritsuk et al. (2007), who carried out simulations of isothermal supersonic turbulence with rms Mach number $\simeq 6$. In accord with the prediction from Eq. (9) the transverse and longitudinal structure functions share a very similar scaling exponent and their ratio is close to 4/3. This is illustrated in more detail in the four panels of Figure 13, where the ratio is plotted explicitly (triangles) as a function of spatial separation and the pre-

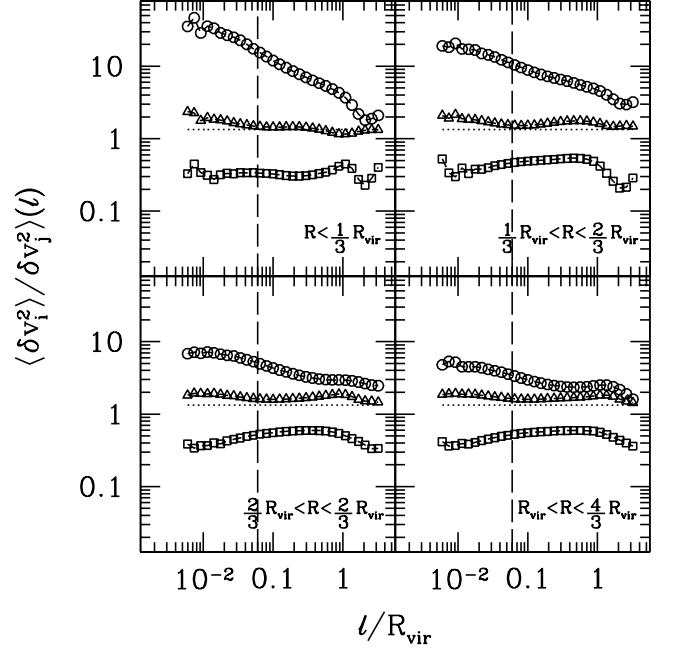


Figure 13. Ratio of second order velocity structure functions: solenoidal-transverse to solenoidal-longitudinal (triangle), compressional-transverse to compressional-longitudinal (squares), and total solenoidal to compressional components (circles), respectively. The dot horizontal line indicates a ratio 0.5, and the vertical dash line a length of 15 resolution elements. The four different panels correspond to the same region around the GC center as in Figure 12.

diction by de Karman & Howarth (1938) is illustrated by the horizontal dotted line. In this figure the vertical line correspond to a separation of 16 resolution elements, roughly the scale where numerical dissipation becomes appreciable. The figure shows that in the core region, on scales where the turbulence motions are resolved, the solenoidal flow is consistent with homogeneous and isotropic turbulence. Anisotropy gradually arises towards the outer regions, and particularly close to the injection scales. This could be related to the fact that in the outer regions the flow becomes increasingly compressional, i.e. the growing presence of shocks which inject turbulence on various scales through the baroclinic term, on timescales comparable to those required to reach isotropization. Note also that anisotropy appears on scales where the turbulence cascade is not resolved, most likely because the longitudinal compression suffers excessive numerical dissipation, which does not affect the relative transverse motions. This means care must be taken when studying anisotropy of turbulent motions on small scales, because it is in general affected by numerical artifacts.

In Figure 13 we also show the ratio of transverse to longitudinal second order structure functions for the compressible velocity (open squares). To the best of our knowledge there is no analytic prediction for this quantity. This ratio is much smaller than for the solenoidal case and it appears to be close to $\frac{1}{2}$, particularly in the outer regions. In other words, the longitudinal term largely dominates the compressional velocity components, which is not surprising because unlike the solenoidal case, longitudinal compression now leads to

dissipation as opposed to excitation of transverse modes.

Finally, note that the turbulent energy is generally dominated by the solenoidal component. This is evident from the plot in Figure 12, and is again illustrated explicitly as a function of separation scale by the open circles in Figure 13 for different regions across the GC. In the core region, $R \leq \frac{1}{3}R_{\text{vir}}$, and at separation scales $\ell \sim \frac{1}{2}R_{\text{vir}}$, the compressional component accounts for about 5% of the total turbulent energy. This value is of course scale dependent, and it rises to a value of order a few close to the injection scale, but drops further towards smaller scales, as a result of the steeper scaling of the compressional versus solenoidal components of the turbulent velocity. However, in the outer region the above ratio at fixed separation scale generally increases, so again at $\ell \sim \frac{1}{2}R_{\text{vir}}$, it reaches values about 20% at the virial and off-virial regions.

We have also carried out the same analysis for density weighted second and third order velocity structure functions, where the velocity is again decomposed according to solenoidal and compressional components. Basically we use the same equations (4)-(6), but with the following substitution $\mathbf{v}_q \leftarrow \rho^\alpha \mathbf{v}_q$, with $\alpha = 1/p$ and p the order of the structure function. This choice of the density weighting corresponds to recent attempts to generalize Kolmogorov's scaling for incompressible to compressible case (e.g. Kritsuk et al. 2009). In any case, the results for the structure function of second and third order are shown in Figure 14, where the black solid line and the different curves and panels have the same meaning as in Figure 12. Basically the density weighted structure functions are consistent with the results presented in Figure 12 for the simple structure functions. If anything, the outer scale where the structure functions flatten and turn over is smaller by a factor $\lesssim 2$ and the slope in the inertial range, although still consistent with K41, is slightly steeper than in the corresponding cases illustrated in Figure 12. However, the structure functions in this case show mild structure both in the inertial range and at the outer scales. This effect, which is most likely attributable to density inhomogeneity, is negligible within $\frac{2}{3}R_{\text{vir}}$, but becomes evident for the virial and off-virial regions.

3.4.1. Convergence

The convergence of numerical results related to the statistical properties of turbulence is well documented in studies of steady-state fully developed turbulence in periodic boxes (Porter et al. 1992, 1994; Federrath et al. 2011). Once steady-state conditions are achieved, the inertial range of the turbulent cascade emerges, provided there is enough separation between the injection and the dissipation scale (e.g., a factor ten). While the former is set by the driving mechanism, and typically acts on scales comparable to the computational domain size, the latter is determined by the dissipation properties of the numerical scheme. In the case of the PPM method, which is commonly employed for compressible turbulence, numerical dissipation affect the turbulent cascade up to separation scales of 32 resolution elements. As a result, on scales of this order and smaller, the turbulence cascade steepens. On larger scales, the cascade is determined by the energy transfer due to nonlinear fluid interactions. As the resolution is increased, numerical

dissipation occurs on smaller spatial scales. Therefore, the inertial range of the turbulence cascade where the nonlinear effects dominate extends to smaller separation scales, while on larger scales its statistical properties remain unchanged (structure function or power spectra). In reality relatively small differences may appear due to temporal fluctuations, particularly on large scales with relatively lower number of degrees of freedom. For this reason, time averaging is also employed.

Guided by the above studies, we try and assess the convergence of the statistical properties of the turbulence in our calculation, by carrying out a lower resolution run which employs 4 instead of 5 levels of refinement. So in this case the resolution inside the GC volume is a factor of two lower. The results are summarized in Fig. 15. Here we compare the structure functions from the low resolution run (dashed line) with those obtained from the fiducial run (solid). We compare by component and by region. So labels s-l, s-t, c-l, c-t in the top-left corner of each subpanel correspond, respectively, to the components: solenoidal-longitudinal (blue), solenoidal-transverse (cyan), compressible-longitudinal (red), compressible-transverse (green); while the labels 0,1,2,3, indicate, respectively, the region: core, off-core, virial and off-virial. Second and third order structure functions are presented in the left and right panel, respectively. For the sake of clarity, structure functions are (partially) compensated, i.e., multiplied by a factor $(\ell/R_{\text{vir}})^{p/3}$, where p is the order, and normalized by a factor, $\langle \delta v_0^p \rangle$, where δv_0 is the velocity increment on scales $\simeq R_{\text{vir}}$, as measured in the fiducial run.

In the low resolution run, 32 resolution elements correspond to a scale, $\ell/R_{\text{vir}} \simeq 0.24$, in Figure 15. Inspection of the various panels in Figure 15 show that in almost all the cases the structure functions from the low resolution and the fiducial run are in good agreement at least on scales a factor two smaller than the one quoted above. This suggests that the fiducial run has definitely reached convergence at the nominal scale of 32 resolution elements, $\ell/R_{\text{vir}} \simeq 0.12$, but that the results are probably fairly reliable also on smaller scales down to $\ell/R_{\text{vir}} \simeq 0.06$.

Perhaps the one exception is for the structure functions of the solenoidal-longitudinal components (s-l) in the core region (0). Here one can observe extra power in the low resolution run compared to the fiducial run, particularly in the third order statistics. This is possibly due to the well known bottleneck effect, whereby the energy transfer due to nonlinear effects becomes inefficient below a certain scale, causing accumulation of kinetic energy on larger scales thereof. To fully address the issue, one would require a calculation with higher resolution than in our fiducial case. We postpone this task to future work. Nevertheless, in terms of convergence of the fiducial run, the above bottleneck effect appears to affect scales smaller than $\ell/R_{\text{vir}} \simeq 0.1$. Intriguingly, the same effect does not appear in the same or any other structure functions computed in the outer parts of the GC volume. If the bottleneck effect is indeed the culprit, one can surmise that its impact becomes less important in the outer regions of the GC, because there more efficient dissipation is provided by the increasing compressional component of the turbulence, which decays through weak shocks.

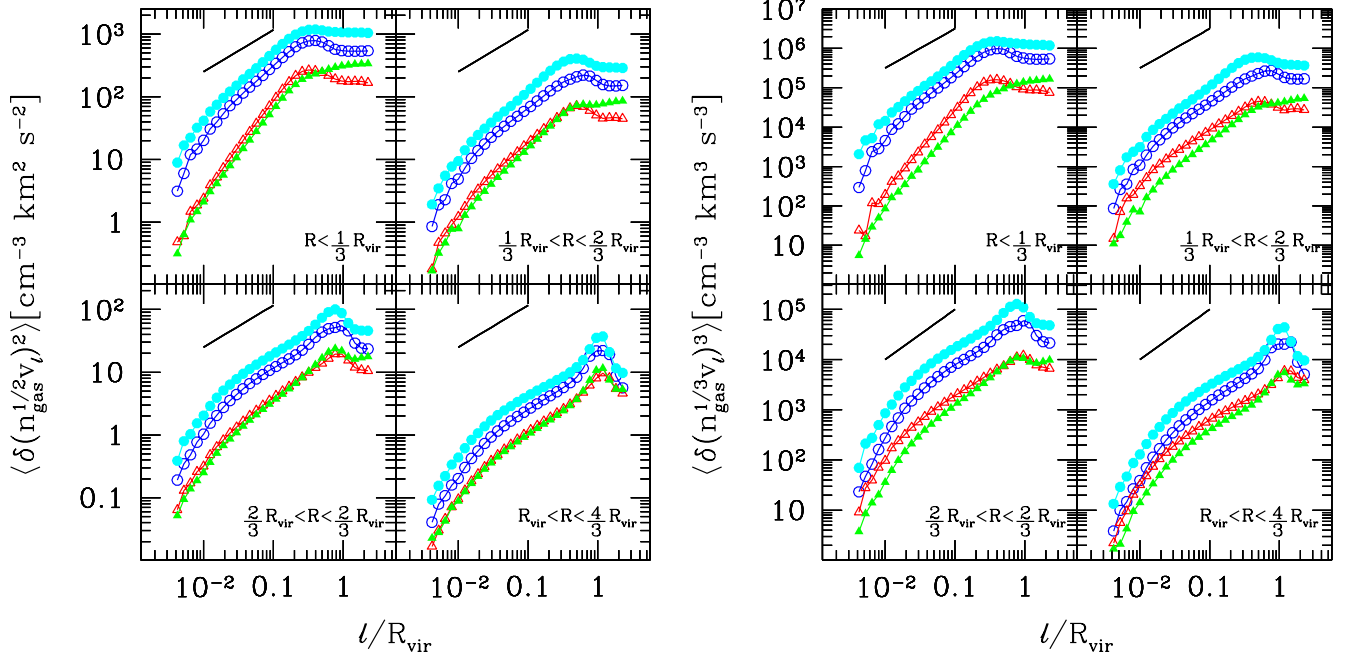


Figure 14. Density weighted second (left) and third (right) order structure function of the velocity field. Different curves from top to bottom correspond to the following components: solenoidal-longitudinal (blue circles), solenoidal-transverse (cyan circles), compressible-longitudinal (red triangles), compressible-transverse (green triangles). The structure functions in the different panels were sampled from different shell volumes centered around the GC center, namely: core corresponding to $R < (1/3)R_{vir}$ (top left), off-core corresponding to $(1/3)R_{vir} < R < (2/3)R_{vir}$ (top right), virial corresponding to $(2/3)R_{vir} < R < R_{vir}$ (bottom left), off-virial corresponding to $R_{vir} < R < (4/3)R_{vir}$ (bottom right).

3.4.2. Comparison with Lagrangian AMR

In Section 3.1.2 we have briefly addressed the difficulty of a Lagrangian AMR approach to study statistical properties of turbulence in the ICM. In particular we have compared a two dimensional density map from our fiducial run employing Eulerian refinement (Figure 3), with a corresponding map obtained from a Lagrangian AMR run with the same initial conditions and the same number of refinement levels (Figure 4). In this section we provide a more quantitative analysis of the results obtained with the two approaches, although not an exhaustive one. In particular, we will compare second and third order structure function computed for different velocity components of the velocity increments and in different volumes of the GC, with and without density weighting. Results for the ordinary structure functions are summarized in Figure 16, which is completely analogous to Figure 15 except that the dashed line now refers to the Lagrangian AMR run. In particular, the solid line refer to our fiducial Eulerian AMR run, the left and right panel correspond to second and third order statistics, and all labels (and colors) have exactly the same meaning.

As for the solenoidal components (s-l and s-t), there is clearly a lack of power of kinetic energy on small scales in the Lagrangian AMR run compared to our fiducial run. The effect becomes more severe towards the outer regions of the GC, consistent with the qualitative impression inferred from the comparison of density maps in Figure 4. In fact, in the outer regions of the GC the mass density is lower and the Lagrangian refinement is less effective. The lack of power on small scale is comparable to, although slightly more pronounced than, in the low resolution run presented in the previous section.

However, on large scales, the structure functions in the Lagrangian AMR run exhibit excess of power with respect to both the fiducial and low resolution runs, so they are qualitatively different. The origin of this feature is not completely clear. However, we suspect that the bottleneck effect is once again at work. Given the relatively low numerical resolution in the outer parts of the GC, the energy cascade through the nonlinear hydrodynamic terms is inefficient, so power of kinetic energy accumulates on large scales. The fact that the issue becomes more visible towards the outer regions supports this conclusion, although (obviously) a more thorough analysis is required for a full understanding.

As for the compressional component, (c-l and c-t), its behavior appears peculiar. Apparently in the core and perhaps even the off-core regions (0,1), the structure functions in the Lagrangian AMR run are characterized by excess of power instead of lack thereof. Towards the outer regions, the imbalance is reversed and both in the virial and off-virial region there is a severe lack of kinetic energy on small scales, as for the solenoidal components. Unlike the solenoidal components, however, we do not see appreciable excess of kinetic energy of compressible motions on large scales. This is perhaps again due to the difference in dissipation mechanism for this component, which decays in significant part through weak shocks.

Finally, in Figure 16 we compare density weighted structure functions computed in Figure 14, with those computed using the Lagrangian AMR run. The comparison shows large discrepancy between results from the two calculations. In particular, in the Lagrangian AMR case the density weighted structure functions always show excess of power at all scales except, occasionally, on the shortest ones (which are not reliable anyway). The rea-

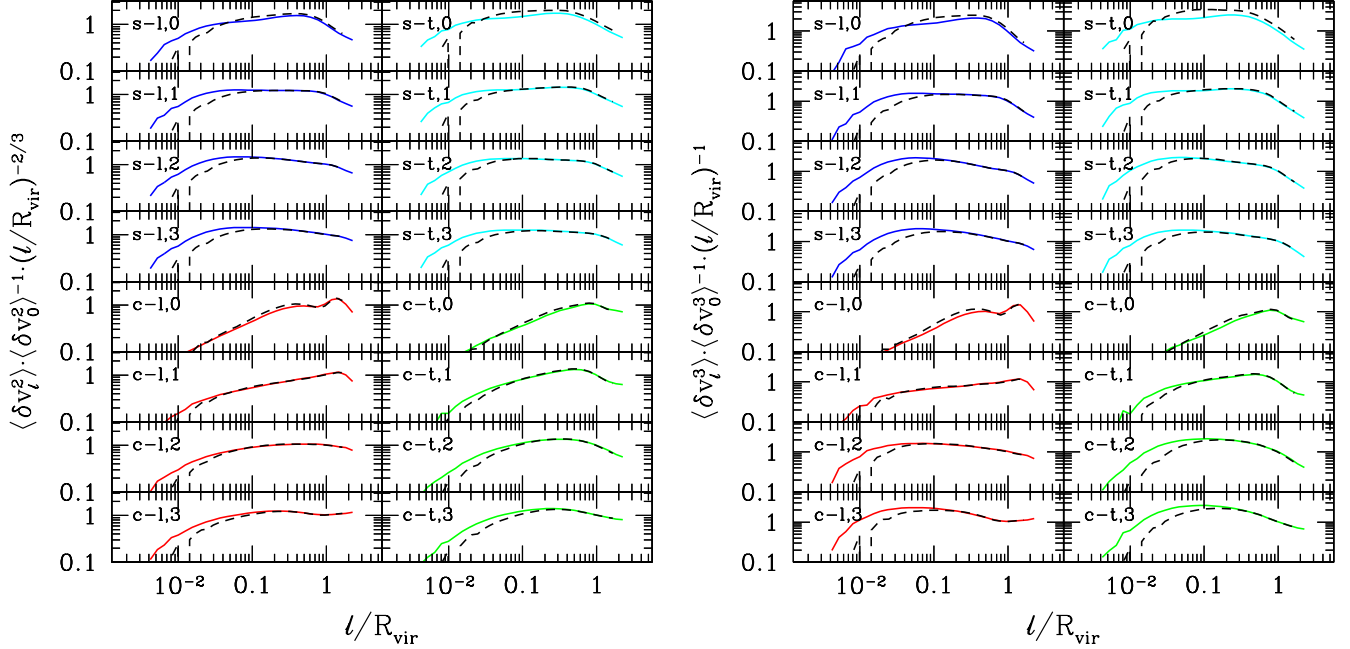


Figure 15. Compensated second (left) and third (right) order structure function of the velocity field from our fiducial run (solid line) and a run at lower resolution by a factor 2 (dashed line). The quantity δv_0 entering the normalization factor corresponds to the velocity increment on scales $\simeq R_{\text{vir}}$, as measured in the fiducial run. Labels s-l,s-t,c-l,c-t indicate, respectively, solenoidal-longitudinal (blue), solenoidal-transverse (cyan), compressible-longitudinal (red), and compressible-transverse (green) component. Labels 0,1,2,3 indicate, respectively, core ($R < (1/3)R_{\text{vir}}$), off-core ($(1/3)R_{\text{vir}} < R < (2/3)R_{\text{vir}}$), virial ($(2/3)R_{\text{vir}} < R < R_{\text{vir}}$), and off-virial ($R_{\text{vir}} < R < (4/3)R_{\text{vir}}$) region.

son for the spurious result is ascribed to the fact that sampling of the velocity field in Lagrangian AMR is already biased towards high density regions. Therefore, when density weighting is applied, the bias becomes even stronger and superlinear. We conclude that the density weighted structure functions applied to data based on Lagrangian adaptivity are not reliable.

4. SUMMARY AND CONCLUSIONS

In this paper we have carried out a numerical study of the turbulence in the ICM of a massive GC. In order to achieve the necessary dynamic range of spatial scales across the GC virial volume, we have employed a novel resolution technique, which we refer to as Eulerian, to distinguish from the mass threshold based Lagrangian refinement criterion. In the Eulerian approach the entire volume occupied by the GC, or at least a large fraction of it, is progressively refined at different stages during its gravitational collapse. This allows us to study in great detail the statistical properties of the turbulence that develops inside the GC volume.

We analyzed the mechanism responsible for injecting the turbulence in the ICM, which we reduce to tidal fields and merging substructures. We estimate the timescale associated with the largest eddy turnover and find it of order the GC crossing or dynamical time, $R_{\text{vir}}/v_{\text{vir}}$. This time is always $\ll H^{-1}(z)$, independent of redshift, so turbulent flows should exist inside collapsed structures independent of redshift. This is confirmed by the large values of the vorticity, even on scales comparable to the virial radius. It is also confirmed by analysis of the structure functions and in particular the ratio of the transverse to longitudinal components of the solenoidal second order structure functions. At least for well resolved scales, this ratio is found in good agreement with analytic pre-

dictions for fully developed isotropic and homogeneous turbulence.

Analysis of the pdf's of the vorticity, velocity divergence and Mach number consistently indicate that the turbulence is compressible but only mildly so. Particular features are recognized in the pdf for the vorticity and velocity divergence that are also seen in dedicated periodic-box simulations of fully developed compressible turbulence.

Intriguingly, shocks are not the only source of vorticity in the ICM, not even the dominant one. In fact the baroclinic term is generated by shocks only in 60% of the cases in the inner $R_{\text{vir}}/3$ and in 40% of the cases beyond that radial distance. In fact, owing to the complex assembly history of its constituent substructures, the presence of internal shocks and lack of complete mixing, the ICM is generally baroclinic and not barotropic, and vorticity arises even in the absence of shocks.

Inspection of the structure functions of second and third order in general indicates that a well defined inertial range of turbulent cascade is established inside the virial volume and even beyond. The injection scale is of order the virial radius, but tends to increase towards the GC outskirts. If we apply a Hodge-Helmholtz decomposition we find that the solenoidal component of the turbulence strongly dominates in the core region, and while still dominating, becomes comparable to the compressible component around the virial radius. In the core region the structure functions for the solenoidal component is well described by a Kolmogorov's spectrum while the structure functions for the compressible component is significantly steeper, close to Burgers' spectrum. In the outer regions the structure functions in general become flatter, indicating perhaps that the turbulence is

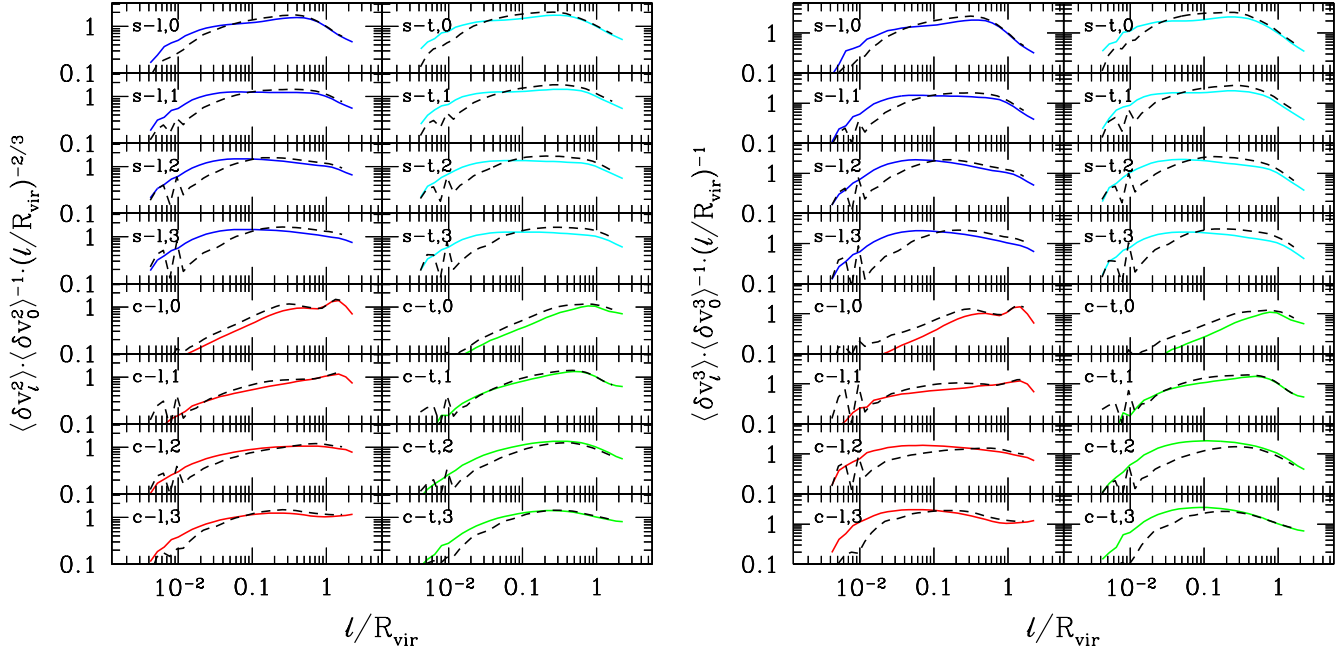


Figure 16. Compensated second (left) and third (right) order structure function of the velocity field from our fiducial run (solid line) and an adaptive-mesh-refinement run (dashed line). The quantity δv_0 entering the normalization factor corresponds to the velocity increment on scales $\simeq R_{\text{vir}}$, as measured in the fiducial run. Labels s-l, s-t, c-l, c-t indicate, respectively, solenoidal-longitudinal (blue), solenoidal-transverse (cyan), compressible-longitudinal (red), and compressible-transverse (green) component. Labels 0,1,2,3 correspond, respectively, core ($R < (1/3)R_{\text{vir}}$), off-core ($(1/3)R_{\text{vir}} < R < (2/3)R_{\text{vir}}$), virial ($(2/3)R_{\text{vir}} < R < R_{\text{vir}}$), and off-virial ($R_{\text{vir}} < R < (4/3)R_{\text{vir}}$) region.

injected on multiple scales.

We have also carried out an identical calculation of the same GC using the same initial conditions, cosmology and finest resolution, but with the AMR technique based on a mass threshold Lagrangian refinement criterion. Compared to our fiducial run, in the Lagrangian AMR case the solenoidal components of ordinary second and third order velocity structure functions lack power on small scales while they exhibit power excess on large scales. These issues become more prominent in the GC outer regions, where the Lagrangian AMR refined volume decreases. The compressional component, on the other hand, shows extra power at all scales in the inner GC regions, and the same severe lack of power at small scales, in the virial region and beyond. The density weighted velocity structure functions extracted from the Lagrangian AMR run, however, appear strongly affected by bias towards high density regions. Therefore, such statistics applied to data based on Lagrangian adaptivity, are not unreliable.

The analysis presented here will be extended to study the statistics of turbulence at different times during the formation history of the cluster. This will help us understand how the turbulence evolves during the cluster formation. The results will be used to understand how the magnetic field grows and, in particular, at what scales we should expect equipartition between magnetic and kinetic energy for given initial conditions as well as to constrain models of acceleration of relativistic electrons in galaxy clusters.

We are grateful to an anonymous referee useful comments that helped improve the manuscript. This work was supported by a grant from the Swiss National Su-

percomputing Center (CSCS) under project ID S275.

REFERENCES

- Beresnyak, A. 2012, *Physical Review Letters*, 108, 035002
- Berger, M. J., & Colella, P. 1989, *JCoPh*, 82, 64
- Bertschinger, E. 2001, *ApJS*, 137, 1
- Biffi, V., Dolag, K., & Böhringer, H. 2011, *MNRAS*, 413, 573
- Biskamp, D. 1993, *Cambridge Monographs on Plasma Physics*, Vol. 1, *Nonlinear Magnetohydrodynamics*, ed. W. Grossman, D. Papadopoulos, R. Sagdeev, & K. Schindler (Cambridge: Cambridge University Press)
- Bodo, G., Cattaneo, F., Ferrari, A., Mignone, A., & Rossi, P. 2011, *ApJ*, 739, 82
- Burgers, J. M. 1939, *Trans. Roy. Neth. Acad. Sci.*, 17, 1
- Chandrasekhar, S. 1951, *Royal Society of London Proceedings Series A*, 210, 26
- Cho, J., & Yoo, H. 2012, *ApJ*, 759, 91
- Churazov, E., Forman, W., Jones, C., Sunyaev, R., & Böhringer, H. 2004, *MNRAS*, 347, 29
- Churazov, E., Forman, W., Vikhlinin, A., Tremaine, S., Gerhard, O., & Jones, C. 2008, *MNRAS*, 388, 1062
- Clarke, T. E. 2004, *Journal of Korean Astronomical Society*, 37, 337
- Clarke, T. E., Kronberg, P. P., & Böhringer, H. 2001, *ApJ*, 547, L111
- Colella, P. 1990, *Journal of Computational Physics*, 87, 171
- de Karman, T., & Howarth, L. 1938, *Royal Society of London Proceedings Series A*, 164, 192
- Dolag, K., Vazza, F., Brunetti, G., & Tormen, G. 2005, *MNRAS*, 364, 753
- Eisenstein, D. J., & Hu, W. 1998, *ApJ*, 496, 605
- Eisenstein, D. J., & Hut, P. 1998, *ApJ*, 498, 137
- Eke, V. R., Navarro, J. F., & Steinmetz, M. 2001, *ApJ*, 554, 114
- Elmegreen, B. G., & Scalo, J. 2004, *ARA&A*, 42, 211
- Enßlin, T. A., & Vogt, C. 2003, *A&A*, 401, 835
- Faltenbacher, A., Kravtsov, A. V., Nagai, D., & Gottlöber, S. 2005, *MNRAS*, 358, 139
- Federrath, C. 2013, *MNRAS*, 436, 1245

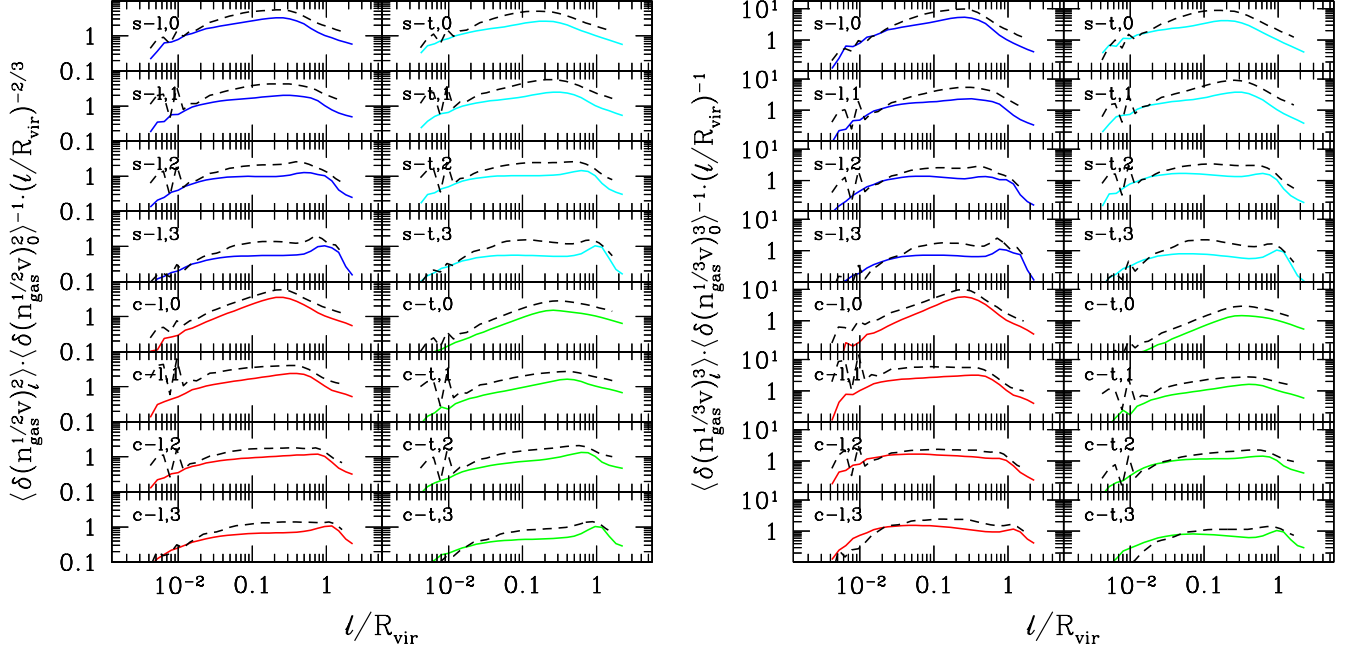


Figure 17. Compensated density weighted second (left) and third (right) order structure function of the velocity field from our fiducial run (solid line) and an adaptive-mesh-refinement run (dashed line). The quantity δv_0 entering the normalization factor corresponds to the velocity increment on scales $\simeq R_{\text{vir}}$, as measured in the fiducial run. Labels s-l,s-t,c-l,c-t indicate, respectively, solenoidal-longitudinal (blue), solenoidal-transverse (cyan), compressible-longitudinal (red), and compressible-transverse (green) component. Labels 0,1,2,3 correspond, respectively, core ($R < (1/3)R_{\text{vir}}$), off-core ($(1/3)R_{\text{vir}} < R < (2/3)R_{\text{vir}}$), virial ($(2/3)R_{\text{vir}} < R < R_{\text{vir}}$), and off-virial ($R_{\text{vir}} < R < (4/3)R_{\text{vir}}$) region.

- Federrath, C., Chabrier, G., Schober, J., Banerjee, R., Klessen, R. S., & Schleicher, D. R. G. 2011, *Physical Review Letters*, 107, 114504
- Federrath, C., Klessen, R. S., & Schmidt, W. 2008, *ApJ*, 688, L79
- Feretti, L., & Johnston-Hollitt, M. 2004, *New Astronomy Reviews*, 48, 1145
- Ginzburg, V. L. 1979, *Theoretical Physics and Astrophysics*, International Series in Natural Philosophy (Oxford: Pergamon)
- Hallman, E. J., & Jeltama, T. E. 2011, *MNRAS*, 418, 2467
- Iapichino, L., & Niemeyer, J. C. 2008, *MNRAS*, 388, 1089
- Iapichino, L., Schmidt, W., Niemeyer, J. C., & Merklein, J. 2011, *MNRAS*, 414, 2297
- Inogamov, N. A., & Sunyaev, R. A. 2003, *Astronomy Letters*, 29, 791
- Kolmogorov, A. 1941a, *Akademiia Nauk SSSR Doklady*, 30, 301
- Kolmogorov, A. N. 1941b, *Akademiia Nauk SSSR Doklady*, 32, 16
- Komatsu, E., Dunkley, J., Nolte, M. R., Bennett, C. L., Gold, B., Hinshaw, G., Jarosik, N., Larson, D., Limon, M., Page, L., Spergel, D. N., Halpern, M., Hill, R. S., Kogut, A., Meyer, S. S., Tucker, G. S., Weiland, J. L., Wollack, E., & Wright, E. L. 2009, *ApJS*, 180, 330
- Konstandin, L., Girichidis, P., Federrath, C., & Klessen, R. S. 2012, *ApJ*, 761, 149
- Kritsuk, A. G., Norman, M. L., & Padoan, P. 2006, *ApJ*, 638, L25
- Kritsuk, A. G., Norman, M. L., Padoan, P., & Wagner, R. 2007, *ApJ*, 665, 416
- Kritsuk, A. G., Ustyugov, S. D., Norman, M. L., & Padoan, P. 2009, in *Astronomical Society of the Pacific Conference Series*, Vol. 406, *Numerical Modeling of Space Plasma Flows: ASTRONUM-2008*, ed. N. V. Pogorelov, E. Audit, P. Colella, & G. P. Zank, 15
- Kuchar, P., & Enßlin, T. A. 2011, *A&A*, 529, A13
- Landau, L. D., & Lifshitz, E. M. 1987, *Course of Theoretical Physics*, Vol. 6, *Fluid Mechanics*, 2nd edn. (Oxford: Pergamon Press)
- Lau, E. T., Kravtsov, A. V., & Nagai, D. 2009, *ApJ*, 705, 1129
- Lazarian, A., Eyink, G. L., & Vishniac, E. T. 2012, *Physics of Plasmas*, 19, 012105
- Lazarian, A., & Vishniac, E. T. 1999, *ApJ*, 517, 700
- Miniati, F., & Colella, P. 2007, *Journal of Computational Physics*, 227, 400
- Miniati, F., & Martin, D. F. 2011, *ApJS*, 195, 5
- Miniati, F., Ryu, D., Kang, H., Jones, T. W., Cen, R., & Ostriker, J. 2000, *ApJ*, 542, 608
- Nagai, D., Vikhlinin, A., & Kravtsov, A. V. 2007, *ApJ*, 655, 98
- Norman, M. L., & Bryan, G. L. 1999, in *Lecture Notes in Physics*, Berlin Springer Verlag, Vol. 530, *The Radio Galaxy Messier 87*, ed. H.-J. Röser & K. Meisenheimer, 106–+
- Oboukhov, A. M. 1941, *Akademiia Nauk SSSR Doklady*, 32, 22
- Parker, E. N. 1958, *Physical Review*, 109, 1874
- Parkin, E. R., & Bicknell, G. V. 2013, *MNRAS*
- Paul, S., Iapichino, L., Miniati, F., Bagchi, J., & Mannheim, K. 2011, *ApJ*, 726, 17
- Porter, D., Pouquet, A., & Woodward, P. 2002, *Phys. Rev. E*, 66, 026301
- Porter, D. H., Pouquet, A., & Woodward, P. R. 1992, *Physical Review Letters*, 68, 3156
- . 1994, *Physics of Fluids*, 6, 2133
- Porter, D. H., & Woodward, P. R. 2000, *ApJS*, 127, 159
- Ryu, D., Kang, H., Cho, J., & Das, S. 2008, *Science*, 320, 909
- Sanders, J. S., Fabian, A. C., & Smith, R. K. 2011, *MNRAS*, 410, 1797
- Sanders, J. S., Fabian, A. C., Smith, R. K., & Peterson, J. R. 2010, *MNRAS*, 402, L11
- Schekochihin, A. A., Cowley, S. C., Kulsrud, R. M., Hammett, G. W., & Sharma, P. 2005, *ApJ*, 629, 139
- Schmidt, W., Collins, D. C., & Kritsuk, A. G. 2013, *MNRAS*, 431, 3196
- Schmidt, W., Federrath, C., Hupp, M., Kern, S., & Niemeyer, J. C. 2009, *A&A*, 494, 127
- Schmidt, W., Kern, S. A. W., Federrath, C., & Klessen, R. S. 2010, *A&A*, 516, A25
- Schuecker, P., Finoguenov, A., Miniati, F., Böhringer, H., & Briel, U. G. 2004, *A&A*, 426, 387
- Subramanian, K., Shukurov, A., & Haugen, N. E. L. 2006, *MNRAS*, 366, 1437
- Sunyaev, R. A., Norman, M. L., & Bryan, G. L. 2003, *Astronomy Letters*, 29, 783
- Valdarnini, R. 2011, *A&A*, 526, A158

- Vazza, F., Brunetti, G., Gheller, C., Brunino, R., & Brüggén, M. 2011, *A&A*, 529, A17
- Vazza, F., Brunetti, G., Kritsuk, A., Wagner, R., Gheller, C., & Norman, M. 2009, *A&A*, 504, 33
- Viallet, M., Meakin, C., Arnett, D., & Mocák, M. 2013, *ApJ*, 769, 1
- Zel'dovich, Y. B., Ruzmaikin, A. A., & Sokoloff, D. D. 1983, *The Fluid Mechanics of Astrophysics and Geophysics*, Vol. 3, *Magnetic Fields in Astrophysics*, 2nd edn., ed. P. H. Roberts (New York: Gordon and Breach)
- Zel'dovich, Y. B., Ruzmaikin, A. A., & Sokoloff, D. D. 1990, *The almighty chance*
- Zhu, W., Feng, L.-L., & Fang, L.-Z. 2011, *MNRAS*, 415, 1093
- Zhuravleva, I., Churazov, E., Kravtsov, A., & Sunyaev, R. 2012, *MNRAS*, 422, 2712
- Zhuravleva, I. V., Churazov, E. M., Sazonov, S. Y., Sunyaev, R. A., & Dolag, K. 2011, *Astronomy Letters*, 37, 141